Author Manuscript

Author Manuscript

Author Manuscript

Author Manuscript

HHS Public Access

Author manuscript

Neuron. Author manuscript; available in PMC 2024 October 18.

Published in final edited form as:

Neuron. 2023 October 18; 111(20): 3211–3229.e9. doi:10.1016/j.neuron.2023.08.023.

Three-dimensional reconstructions of mechanosensory end organs suggest a unifying mechanism underlying dynamic, light touch

Annie Handler[1,2,7], **Qiyu Zhang**[1,2,7], **Song Pang**[3,5], **Tri M. Nguyen**[1], **Michael Iskols**[1,2], **Michael Nolan-Tamariz**[1,2], **Stuart Cattel**[1,2], **Rebecca Plumb**[1,2], **Brianna Sanchez**[1,2], **Karyl Ashjian**[1,2], **Aria Shotland**[1,2], **Bartianna Brown**[1,2], **Madiha Kabeer**[1,2], **Josef Turecek**[1,2], **Michelle M. DeLisle**[1,2], **Genelle Rankin**[1,2], **Wangchu Xiang**[1,2], **Elisa C. Pavarino**[1,2], **Nusrat Africawala**[1,2], **Celine Santiago**[1,2], **Wei-Chung Allen Lee**[1,4], **C. Shan Xu**[3,6], **David D. Ginty**[1,2,8,*]

[1]Department of Neurobiology, Harvard Medical School, 220 Longwood Avenue, Boston, MA 02115, USA

[2]Howard Hughes Medical Institute, Harvard Medical School, 220 Longwood Avenue, Boston, MA 02115, USA

[3]Janelia Research Campus, Howard Hughes Medical Institute, Ashburn, VA 20147, USA.

[4]F.M. Kirby Neurobiology Center, Boston Children's Hospital, Boston, MA, USA

[5]Current address: Yale School of Medicine, New Haven, CT 06510, USA

[6]Current address: Department of Cellular & Molecular Physiology, Yale School of Medicine, New Haven, CT 06510, USA

[7]These authors contributed equally.

[8]Lead contact

SUMMARY

Across mammalian skin, structurally complex and diverse mechanosensory end organs respond to mechanical stimuli and enable our perception of dynamic, light touch. How forces act

[*]Correspondence: david_ginty@hms.harvard.edu.

AUTHOR CONTRIBUTIONS

AH, QZ, SP, CSX, and DDG conceived the study. AH and QZ, with the help of MI, MNT, and SC, prepared all EM samples. SP and CSX prepared and imaged FIB-SEM samples. Post data registration and supervision of FIB-SEM samples, CSX. Global image alignment and processing, QZ and AH. Network training and automatic segmentation, TMN under the supervision of WCAL. Ground truth for FIB-SEM volumes was annotated by RP, BS, KA, AS, BB, MK, NA, SC, AH, and QZ. Model proofreading, AH, QZ, and MNT. Figure S1A, AH. Figures S1B, S1C, and 2A–E, JT. Open field and balance beam behavior assays, MD. Preliminary experiments related to study, WX, ECP, SC, GR, and CS. AH and DDG wrote the paper with input from all authors.

DECLARATION OF INTERESTS

C.S.X. is the inventor of a US patent assigned to HHMI for the enhanced FIB-SEM systems used in this work: Xu, C.S., Hayworth K.J., Hess H.F. (2020) Enhanced FIB-SEM systems for large-volume 3D imaging. US Patent 10,600,615, 24 Mar 2020. The other authors declare no competing interests.

Publisher's Disclaimer: This is a PDF file of an unedited manuscript that has been accepted for publication. As a service to our customers we are providing this early version of the manuscript. The manuscript will undergo copyediting, typesetting, and review of the resulting proof before it is published in its final form. Please note that during the production process errors may be discovered which could affect the content, and all legal disclaimers that apply to the journal pertain.

Author Manuscript Author Manuscript Author Manuscript Author Manuscript

on morphologically dissimilar mechanosensory end organs of the skin to gate the requisite mechanotransduction channel Piezo2 and excite mechanosensory neurons is not understood. Here, we report high-resolution reconstructions of the hair follicle lanceolate complex, Meissner corpuscle, and Pacinian corpuscle and the subcellular distribution of Piezo2 within them. Across all three end organs, Piezo2 is restricted to the sensory axon membrane, including axon protrusions that extend from the axon body. These protrusions, which are numerous and elaborate extensively within the end organs, tether the axon to resident non-neuronal cells via adherens junctions. These findings support a unified model for dynamic touch in which mechanical stimuli stretch hundreds to thousands of axon protrusions across an end organ, opening proximal, axonal Piezo2 channels and exciting the neuron.

In Brief

Handler and Zhang et al. show restricted subcellular localization and function of Piezo2 to the sensory axons of mechanosensory end organs and through high-resolution FIB-SEM, they reveal a conserved ultrastructural anchoring motif shared by end organs involved in dynamic, light touch. These findings suggest a unified model of mechanotransduction.

Graphical Abstract

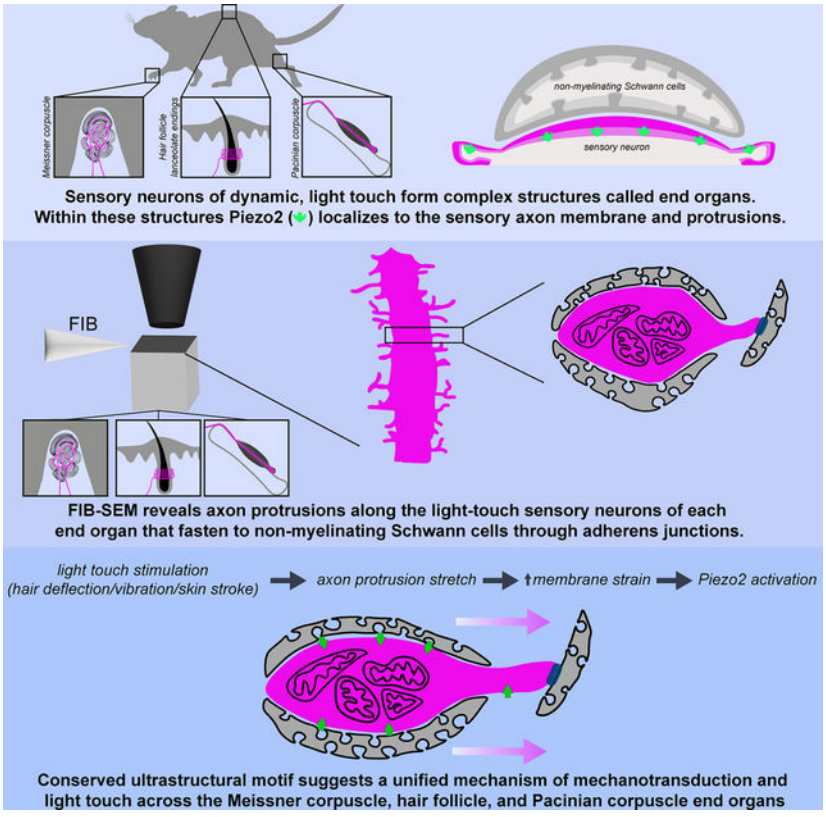

Author Manuscript Author Manuscript Author Manuscript Author Manuscript

INTRODUCTION

Our perception of light touch is initiated by activation of mechanically sensitive low-threshold mechanoreceptors (LTMRs) whose endings in the skin associate with non-myelinating Schwann cells and other cell types to form complex terminal structures called mechanosensory end organs. The cell bodies of these light touch mechanosensory neurons reside within the dorsal root ganglia (DRG) and trigeminal ganglia and extend a peripherally-projecting axon that terminates within a peripheral end organ and a second, centrally-projecting axon that extends into the spinal cord or brainstem. Thus, forces generated by tactile stimuli impinging on the skin surface activate the end organs, where mechanical forces are converted to electrical signals that are propagated along the LTMR axon to the spinal cord and brainstem. Although the structural diversity of mechanosensory end organs has been appreciated for nearly two centuries and has long been thought to underlie the distinct tuning properties of LTMR subtypes,[1] how forces acting on these structurally dissimilar end organs lead to mechanotransduction has remained unclear.

The sensory neurons of touch can be classified based on their electrophysiological properties, including conduction velocity (Aβ-, Aδ-, and C-fiber) and force-threshold for activation (low or high threshold). Our sense of discriminative light touch arises predominantly from the fast conducting, Aβ low-threshold mechanoreceptors (Aβ LTMRs), which are activated by indentation forces as low as 0.5–2 mN.[2–8] The Aβ LTMRs can be subdivided by their rate of adaptation, with slowly adapting (SA) neurons firing throughout the duration of static indentation,[9–12] and rapidly adapting (RA) neurons firing only 1–2 action potentials during the onset and offset of a step indentation.[13,14] Aβ LTMRs are further distinguished by their vibration tuning and receptive field properties. Indeed, in glabrous (non-hairy) skin, there are two distinct Aβ RA-LTMR subtypes that are optimally sensitive to either low frequency vibrations (40–100 Hz) and exhibit small receptive fields, or instead uniquely sensitive to higher frequencies (>200 Hz) and exhibit expansive receptive fields.[1,3,15–18] This difference in vibration tuning is thought to arise from the dissimilar end organ structures formed by these two Aβ RA-LTMRs subtypes. On the other hand, the Aβ SA-LTMRs of hairy and glabrous skin have small receptive fields and, although Aβ SA-LTMRs are sensitive to vibratory stimuli, these neurons exhibit minimal frequency tuning.[1,18] These distinctions in physiological and receptive field properties of Aβ LTMR subtypes have led to the suggestion that while Aβ SA-LTMRs report pressure, points, and edges within their receptive fields, the Aβ RA-LTMRs are uniquely suited to report dynamic tactile stimuli.

The unique physiological properties of Aβ LTMR subtypes is reflected in their distinct end organ structures. Aβ SA-LTMRs innervate both hairy and glabrous skin types to form Merkel cell-neurite complexes at the dermal-epidermal boundary.[19,20] Aβ RA-LTMR subtypes also innervate both skin types, forming longitudinal lanceolate endings that run parallel to the shaft of hair follicles in hairy skin,[8,21–24] and Meissner corpuscles (low frequency tuned and small receptive field) and Pacinian corpuscles (high frequency tuned with a large receptive field) located in glabrous skin, or in the deep dermis and associated with bones, respectively.[14,25] Despite the overall distinct morphologies of the Aβ RA-LTMRs associated with hair follicles, Meissner corpuscles, and Pacinian

Author Manuscript Author Manuscript Author Manuscript Author Manuscript

corpuscles (Figure 1A), the observation that the Aβ RA-LTMRs of these three structures are highly sensitive and tuned to vibrotactile stimuli (Figures S1A–S1C) suggests a conserved mechanotransduction mechanism underlying dynamic, light touch. In addition to the ultrasensitive Aβ RA-LTMRs that innervate hair follicles and corpuscles, additional LTMR subtypes that are less sensitive to tactile stimuli also terminate within these structures. This includes Aβ field-LTMRs,[2] which form circumferential endings that wrap around hair follicles distal to the lanceolate complexes, and Ret-positive (Ret^+) Aβ LTMRs that innervate Meissner corpuscles alongside the more sensitive TrkB-positive ($TrkB^+$) Aβ RA-LTMR.[3] The basis for the varied mechanosensitivity of Aβ LTMR subtypes both across distinct end organs and even within the same end organ remains an outstanding question.

Remarkably, despite the wide range of physiological and morphological properties across the mechanosensory neurons, Piezo2 has emerged as the principal, requisite mechanosensitive channel for LTMR subtypes.[26–34] Indeed, mice and humans lacking Piezo2 exhibit profound deficits in light touch sensation.[26–30,35,36] While the terminal structure of the Merkel cell-neurite complex formed by Aβ SA-LTMRs is relatively simple and the mechanism by which force activates Piezo2 within this complex is well studied,[35–39] the basis for how forces activate Piezo2 in the more complex end organ structures formed by the Aβ RA-LTMR subtypes that underlie dynamic, light touch—including hair follicle lanceolate complexes, Meissner corpuscles, and Pacinian corpuscles, remains unknown. Here, we report large-scale, high resolution 3D EM reconstructions of these three Aβ RA-LTMR end organs and the subcellular distribution of Piezo2 within them. Our findings reveal a unified model of mechanotransduction within the mechanosensory end organs of dynamic, light touch.

RESULTS

Piezo2 localization across three Aβ RA-LTMR end organ structures

We first localized Piezo2 within the end organs innervated by Aβ RA-LTMRs—the guard hair follicle, Meissner corpuscle, and Pacinian corpuscle. We generated a knock-in mouse in which a “spaghetti monster-FLAG” (smFP-FLAG) epitope tag[40] is fused to the carboxy terminal end of the Piezo2 protein (*Piezo2*$^{smFP\text{-}FLAG}$ mice; Figure 1B) to enable specific, high affinity immunolocalization of endogenous Piezo2. The multimerized FLAG epitope inserted into the scaffold of GFP proved beneficial in enhancing the signal-to-noise in detecting Piezo2 in the skin beyond what was possible with a published Piezo2 reporter line[26,36] and appeared to have no effect on general ambulatory behavior in homozygous transgenic animals, suggesting conserved function of the Piezo2 channel (Figures S1D and S1E). When hairy and glabrous skin of *Piezo2*$^{smFP\text{-}FLAG}$ mice were co-stained with anti-FLAG and anti-neurofilament heavy chain (NFH, a reporter for Aβ axons), we observed spatial colocalization of Piezo2-FLAG and NFH in Aβ sensory axons forming lanceolate and circumferential endings around hair follicles and along the Aβ sensory axons innervating the Meissner corpuscles in glabrous skin and Pacinian corpuscles associated with bone (Figures 1B, S1F and S1G). While Piezo2 was localized to the terminal portion of Aβ axons forming the end organ structures, it was noticeably absent from NFH^+ axon fibers before they entered the end organ structures (Figures 1B). Piezo2 was also

Author Manuscript Author Manuscript Author Manuscript Author Manuscript

absent from resident non-myelinating Schwann cells, most easily appreciated by the lack of Piezo2-FLAG labeling in the $S100^+$ and PLP^{EGFP+} lamellar cells within the Meissner and Pacinian corpuscles, respectively (Figures S1F). Strikingly, we found small $Piezo2^+$, spine-like protrusions (~1 μm in length) that emanated from the NFH^+ axons (Figures S1F) forming the lanceolate endings, Meissner corpuscles, and Pacinian corpuscles, hinting at the presence of a conserved ultrastructural feature of Aβ RA-LTMRs that may be involved in mechanotransduction.

Within each mechanosensory end organ, Aβ RA-LTMR axons associate with non-myelinating Schwann cells, referred to as terminal Schwann cells (TSCs) in hairy skin and lamellar cells in Meissner corpuscles and Pacinian corpuscles. Whether TSCs and lamellar cells serve as passive modulators of mechanical forces impinging on the sensory axon or play an active role in initiating mechanical responses is an area of active investigation.[41–43] Deleting Piezo2 in both somatosensory neurons and non-neuronal cells leads to complete loss of light touch responses measured in the DRG, spinal cord, and brainstem, emphasizing the critical role of Piezo2 in light touch.[29,30] However, definitively answering whether Piezo2 is expressed and functions within the axon terminals or non-neuronal cells requires a high-resolution Piezo2 localization approach and physiological analyses of mice lacking Piezo2 only in non-neuronal cells. Therefore, we next performed immunoelectron microscopy with samples from *Piezo2*$^{smFP\text{-}FLAG}$ animals to determine the cell-type specific and subcellular localization of Piezo2 within the end organs. We observed Piezo2-FLAG enriched along the sensory axon membranes in all three end organs (Figures 1C and S2A), consistent with our light microscopy findings. Piezo2-FLAG was localized to Aβ RA-LTMR membranes of hair follicle lanceolate endings, Aβ field-LTMR circumferential endings surrounding hair follicles, and Aβ LTMR terminals in Meissner corpuscles and Pacinian corpuscles (Figures 1C and S2A). Similar to the $Piezo2^+$ spine-like processes observed by light-microscopy, we also observed Piezo2-FLAG localization along small protrusions that extend beyond the main body of the Aβ LTMR axons (Figures 1C and S2A), suggesting that these curious finger-like structures—first described over fifty years ago[23,44–47]—may participate in mechanical gating of the channel. Subcellular quantification of puncta density and size across end organs revealed that unlike the select enrichment of Piezo2-puncta along the sensory axon membrane of Piezo2-FLAG animals, little if any immunostaining signal colocalized to the membranes of TSCs and lamellar cells above the level of background staining observed in non-transgenic controls (Figures 1C–D and S2A–S2D). Consistent with this observation, electrophysiological recordings in *Dhh-Cre; Piezo2*$^{f/f}$ mice showed that deleting Piezo2 in TSCs and lamellar cells, but not in neurons, did not affect mechanosensitivity or response properties of Aβ mechanosensory neurons (Figures 2A–E). This is in contrast to the near-complete loss of low-threshold responses in *Cdx2-Cre; Piezo2*$^{f/f}$ mice, which lack Piezo2 in both somatosensory neurons and non-neuronal cells (Figures 2B). This dramatic difference in tactile sensitivity is mirrored at the behavioral level, where deletion of Piezo2 in Dhh^+ Schwann cells has little effect on general ambulatory behavior while deletion of Piezo2 in sensory neurons leads to severe motor deficits (Figures S3A and S3B). Taken together, our light microscopy, immuno-EM, and genetic manipulations and electrophysiological findings indicate that in all three end

Author Manuscript Author Manuscript Author Manuscript Author Manuscript

organs the Aβ RA-LTMR sensory axon serves as the main site of Piezo2-dependent mechanotransduction, consistent with previously published data.[26,27,48,49]

FIB-SEM volumes of three Aβ RA-LTMR end organs

Key insights into mechanotransduction in the cochlea were revealed by classical 3D scanning electron microscopy analysis of cochlear hair cells. This 3D analysis led to the discovery of hair cell stereocilia tip links that bridge stereocilia and the widely accepted model for how mechanical forces generated by stereocilia movement are transduced into channel gating and hair cell depolarization.[50–52] In an attempt to gain a comparable level of insight for tactile sensory neurons, we visualized the 3D architecture of the three Aβ RA-LTMR end organs in their native tissue context to identify ultrastructural features that may underlie mechanotransduction across these morphologically dissimilar Aβ LTMR end organs. For this, we applied enhanced Focused Ion Beam Scanning Electron Microscopy (FIB-SEM)[53] to image the three end organs in their entirety with 6-nm isotropic voxels (Figures 3A–D). Coupled with deep-learning based segmentation,[54] we reconstructed the Aβ RA-LTMR axons of a guard hair lanceolate complex, two Meissner corpuscles, and a Pacinian corpuscle to generate high resolution 3D renderings of these Aβ RA-LTMR end organs.

3D architecture of the guard hair lanceolate complex

In hairy skin, we imaged a 5.12×10^5 μm^3 volume of tissue containing the entire Aβ RA-LTMR lanceolate complex surrounding a guard hair follicle, which is the longest hair type on the mouse trunk and accounts for 1% of all trunk hair follicles (Figure 3A). We identified and reconstructed all 47 lanceolate endings formed by heavily myelinated Aβ axons that encircle the outer root sheath of the hair follicle (Figure 4A and Video S1). We presume these to be the endings of two or three Aβ RA-LTMR neurons based on prior anatomy experiments.[8,55] All but one axon branched at the base of the hair follicle complex to form multiple interdigitated lanceolate endings that extend within the longitudinal collagen matrix along the length of the hair shaft. In addition to the 47 Aβ RA-LTMR lanceolate endings, we were surprised to find six lanceolate endings formed by four unmyelinated, small caliber axons (Figure S4A). Smaller diameter Aδ- and C-LTMRs also form lanceolate endings associated with awl/auchene and zigzag hair follicles but not guard hair follicles;[8] however, CGRP antibody staining in hairy skin revealed $CGRP^+$, NFH^- lanceolate endings (Figure S4B), suggesting that small diameter, $CGRP^+$ fibers may form a small subset of lanceolate endings surrounding hair follicles. Each lanceolate ending was associated with processes originating from 1–3 of the 17 TSCs, which were also embedded within the longitudinal collagen matrix and were fully reconstructed. These 17 TSCs were mostly non-overlapping, tiling the hair follicle, and had cell bodies located at the base of the lanceolate complex (Figure 4D and Videos S2 and S3), consistent with a previous report.[21] Although the TSC processes formed an overlay that covered the lanceolate axons along their full extension adjacent to the hair shaft, intermittent gaps in TSC coverage formed at the boundaries of TSC processes, leaving exposed small portions of axon membrane along the full length of the lanceolate complex. These gaps most often formed on opposite sides of the lanceolate ending, along the axon membrane proximal and distal to the outer root sheath (Figures 4A and S4C). The membranes of TSCs were studded with membrane pits that appeared

Author Manuscript Author Manuscript Author Manuscript Author Manuscript

structurally analogous to lipid-raft structures called caveolae, which are found in several cell types, including skeletal and endothelial cells.[56] Indeed, deletion of the *Caveolin1* gene led to loss of these structures within TSCs of hairy skin (Figures S4C and S4D).

Distal to the outer root sheath and longitudinal collagen network lies the circumferential collagen matrix that encircles the hair shaft at an orientation perpendicular to the longitudinal collagen network and contains the circumferential endings of the Aβ field-LTMRs and $CGRP^+$ Aδ circumferential-high threshold mechanoreceptors (Aδ circ-HTMRs).[2,57,58] These two circumferential sensory neurons are distinct from Aβ RA-LTMRs not just in their perpendicular orientation to the lanceolate endings, but also in their mechanical tuning properties. While Aβ field-LTMRs are sensitive to gentle stroking across the skin, both circumferential ending neuron types exhibit a higher activation threshold in response to skin indentation when compared to Aβ RA-LTMRs.[2,57,59] Within the volume, we identified and reconstructed two large caliber, myelinated axons we presume to be Aβ field-LTMRs, and we reconstructed a subset of circumferential TSCs that associated with these large caliber axons (Figures 4B and 4E and Video S4). We also reconstructed two small diameter axons within the circumferential collagen matrix that have morphological properties of circumferential $CGRP^+$ Aδ circ-HTMR endings (Figures 4C and S4E and Video S5). The designation of Aβ field-LTMRs and $CGRP^+$ Aδ circ-HTMRs in our volume was further validated in parallel by genetically labeling each subtype with an EM reporter[60] and identifying ultrastructural homology by single section transmission electron microscopy (TEM) (Figure S4F). Indeed, by TEM, we observed abundant neurofilaments in Aβ field-LTMRs that were noticeably absent from small diameter $CGRP^+$ Aδ circ-HTMRs, an ultrastructural distinction also observed between the two classes of circumferential endings in our FIB-SEM volume. In addition to the sensory axons and TSCs within the circumferential collagen, we found an extensive network of ~17 non-neuronal cells, which we term circumferential support cells (CSCs). These previously uncharacterized CSCs were structurally distinct from TSCs in their minimal association with circumferential sensory axons. We reconstructed a subset of CSCs whose cell bodies reside in the circumferential collagen network distal to the lanceolate complexes and found that they fully encircle the guard hair in a vertically tiled manner (Figure 4F and Video S6).

To identify structural features underlying the heightened sensitivity of Aβ RA-LTMRs to mechanical forces, we examined features unique to the Aβ RA-LTMR lanceolate complexes. One strikingly unique ultrastructural feature of the Aβ RA-LTMRs was the presence of numerous axon protrusions that emerged only where the sensory axon formed close associations with TSCs (Figures 5A–C), a location coincident with the axolemmal expression of Piezo2 (Figures 1B and S1F). These axon protrusions appeared along the length of lanceolate endings at a density of 1.9 protrusions/μm of axon and extended through the intermittent gaps between TSC processes (Figures 5B–C). Moreover, protrusions were absent from the TSC gaps proximal to the outer root sheath epithelial cells (Figure 5C) and were sparse or lacking in both the six small caliber lanceolate endings and the circumferential endings of Aβ field-LTMRs and $CGRP^+$ Aδ circ-HTMRs (Figures S4A and S5A). Of the 1,742 axon protrusions originating from the 47 Aβ RA-LTMR lanceolate endings, 51% (880/1742) reached beyond the local longitudinal collagen matrix and extended into the circumferential collagen network (Figures 5D and S5B). Because

Author Manuscript Author Manuscript Author Manuscript Author Manuscript

of the potential for unique biomechanical properties at the longitudinal/circumferential collagen matrix interface during mechanical stress, we examined the properties of the axon protrusions that extended across the interface and into the circumferential collagen region. We found that 57.3% (504/880) of these axon protrusions formed close associations with resident cells of the circumferential collagen matrix (Figures 5D, 5E and S5B). Furthermore, a significant proportion (32%, 163/504) of these contacts formed with the four reconstructed CSCs (Figures 5E and Video S7). In contrast, only a single contact was observed between the axon protrusions and the seven reconstructed circumferential TSCs (Figure S5C), revealing a preferential association between the axon protrusions and CSCs. These findings suggest that an extensive series of contacts between Aβ RA-LTMR lanceolate axon protrusions and CSCs serve to bridge the Aβ lanceolate endings across two perpendicularly oriented collagen matrices and anchor the sensory axon within the circumferential collagen region. We also observed lanceolate ending axon protrusions that contact non-neuronal cells within the circumferential collagen network of non-guard hairs, most of which are innervated exclusively by Aδ-LTMRs and C-LTMRs (Figure S5D). This ultrastructural motif conserved across LTMRs that form lanceolate endings around hair follicles suggests a model in which hair deflection or local skin indentation moves the circumferential collagen matrix relative to the longitudinal collagen matrix, thereby stretching axon protrusions and gating Piezo2 localized within the axon membrane of lanceolate endings.

3D architecture of the Meissner corpuscle

We next sought to determine whether similar ultrastructural features are prevalent in other Aβ RA-LTMR end organs and, if so, whether a common model may explain mechanotransduction across them. Therefore, we imaged a 5.6×10^4 μm^3 volume of glabrous skin containing a Meissner corpuscle innervated by two myelinated Aβ LTMRs (Figures 3B and 6A and Video S8). We reconstructed these two Aβ LTMRs innervating the Meissner corpuscle, in addition to their associated lamellar cells and a subset of unmyelinated axons associated with the corpuscle, which may correspond to peptidergic and non-peptidergic C-fibers (Figures 6A–C and S6A).[61] By confocal microscopy, the Meissner corpuscle appears as a spherical end organ with tortuous NFH$^+$ axons (Figure 1A). However, our reconstruction revealed two Aβ LTMR axons that traveled through the corpuscle in a largely linear manner (Figures 6A and 6B), remarkably analogous in appearance to the hair follicle-associated Aβ RA-LTMR lanceolate endings (Figure 5A). While the central Meissner Aβ axon was unbranched and shed its myelin at the base of the corpuscle structure, the more apical Aβ axon branched earlier within the dermal papilla and continued unmyelinated for 27.4 μm before entering the corpuscle (Figure 6A). Four lamellar cells with cell bodies situated at the edge of the corpuscle extended numerous interdigitated lamellar processes to form the characteristic multi-layered wrappings of Meissner Aβ LTMRs (Figure 6C). Three of the four lamellar cells contributed to the innermost wrapping of both Aβ LTMR axons, revealing a high degree of interconnectedness of axons and lamellar cells within this structure (Figure 6C). As with the TSCs of hairy skin, caveolae appeared along the lamellar cell membrane; these were absent in mice lacking the *Caveolin1* gene (Figure S6B), revealing a conserved structural feature of TSCs of hair follicles and lamellar cells of Meissner corpuscles. Moreover, as with hair follicle TSCs, the corpuscle's

Author Manuscript Author Manuscript Author Manuscript Author Manuscript

lamellar cells had intermittent gaps in coverage along the sensory axon body (Figures 6C and S6C). These gaps often appeared at the vertices of the ellipsoid axon profile and their position remained consistent across the corpuscle. Strikingly similar to what we observed for hair follicle Aβ RA-LTMR lanceolate endings, an extensive array of axon protrusions emerged between these gaps and extended into the surrounding collagen network (Figure 6C). These protrusions were restricted to the portion of axon within the corpuscle proper, suggestive of a role in mechanotransduction given their proximity to membrane-bound Piezo2 (Figures 1C, 6A–C, S1F and S2A).

Within most Meissner corpuscles exist two molecularly and physiologically distinct Aβ LTMRs.[3] The TrkB$^+$ Meissner afferent is the stereotypical, highly sensitive Aβ RA-LTMR, while the Ret$^+$ Meissner afferent is, on average, less sensitive to skin indentation and exhibits varying rates of adaptation.[3] In addition to being molecularly and physiologically distinct, these two neuronal populations have distinct interactions with lamellar cells. Previous work detailing ultrastructural distinctions across the two Meissner afferent subtypes found that lamellar cell processes associated with the axons of TrkB$^+$ Aβ RA-LTMRs were more elaborate and numerous than those associated with Ret$^+$ Aβ LTMRs.[3] In our 3D reconstruction, we found that across all depths of the corpuscle, the central axon (Figure 6C and S6E, magenta) was wrapped more extensively by lamellar cell processes, suggestive of the central axon being TrkB$^+$ and the peripheral axon being Ret$^+$.

Using this classification for the two axons, we analyzed the axon protrusion density across these two subtypes. We found that the putative TrkB$^+$ Aβ RA-LTMR axon formed more than twice as many axon protrusions as the putative Ret$^+$ axon (396 and 162, respectively) and had 11.7 protrusions/μm of axon—a density roughly 4 times that of the putative Ret$^+$ axon (3.0 protrusions/μm), revealing a second ultrastructural distinction for these two subtypes that may underlie their difference in tactile sensitivity (Figure 6D). To test whether the density of axon protrusions along TrkB$^+$ axons was consistent across corpuscles, we reconstructed the Aβ axon of a second, singly innervated Meissner corpuscle from a different FIB-SEM volume (Figures 3C and S6D). As at least 80% of corpuscles within the forepaw digits receive a TrkB$^+$ afferent (Figure S6F), and because Meissner corpuscles are virtually absent in sensory neuron-specific TrkB knock-out mice,[3] we presumed that the axon of this singly innervated Meissner corpuscle was TrkB$^+$. We found that the presumed TrkB$^+$ afferent of the singly innervated Meissner corpuscle was centrally located in the corpuscle and wrapped by numerous lamellar cell processes—features paralleled by the TrkB$^+$ axon of the dual-innervated Meissner corpuscle (Figure S6D and S6E). Moreover, the axon of the singly innervated Meissner corpuscle had a density of 15.1 protrusions/μm of axon, a value comparable to the TrkB$^+$ axon of the dual-innervated Meissner (Figure 6D). Importantly, in characterizing the terminal structure of the axon protrusions from both corpuscles, we observed a conserved structural motif analogous to Aβ RA-LTMR hair follicle lanceolate endings. We found that 62% (334/538) and 67% (264/396) of protrusions from the presumed TrkB$^+$ axon of the single and dual-innervated Meissner corpuscles, respectively, contacted lamellar cell processes within the corpuscle (Figure 6D and Video S9). Although the density of protrusions was lower in the presumed Ret$^+$ axon of the dual-innervated Meissner corpuscle, a similar proportion of its protrusions formed intimate associations with lamellar cells (60%, 97/162) (Figure 6D). The heightened density of axon

Author Manuscript Author Manuscript Author Manuscript Author Manuscript

protrusions in the more mechanically sensitive TrkB$^+$ Aβ RA-LTMRs, compared to the Ret$^+$ Aβ LTMR, suggests that these structures and their contacts throughout the end organ structure may contribute to the high sensitivity and low activation threshold of TrkB$^+$ Aβ RA-LTMR axons of Meissner corpuscles, in a manner analogous to the lanceolate endings of hair follicles.

3D architecture of the Pacinian corpuscle

The third end organ structure innervated by Aβ RA-LTMRs, the Pacinian corpuscle, is altogether unique in its size, location, simplicity in morphological appearance, and sensitivity to high frequency vibrations. Pacinian corpuscles of the mouse are mostly restricted to the periosteum surrounding bone and are 200–300 μm in length and ~40 μm in diameter (Figure 1A).[62,63] Each Pacinian corpuscle is innervated by a single Aβ RA-LTMR axon that extends the length of the corpuscle, typically unbranched, before terminating in a branched, bulbous structure called the ultraterminal region.[63] Encircling the central axon are numerous concentric cellular processes formed by non-neuronal cells.[46] The innermost rings that form the inner core around the axon are established by lamellar cells analogous to those of the Meissner corpuscle.[64] Although the Aβ LTMR of the Pacinian is analogous to the Aβ lanceolate ending and Meissner afferents in its RA response to static indentation, it is unique in its sensitivity to high frequency vibrations (>200 Hz).[15,16] To visualize the 3D ultrastructural features of the Pacinian Aβ RA-LTMR, we imaged a 9.6×10^5 μm volume of tissue isolated from the periosteum membrane surrounding the fibula of a mouse and containing a Pacinian corpuscle (Figure 3D). We identified and reconstructed a single Aβ RA-LTMR axon that shed its myelin upon entering the corpuscle and remained unbranched within the terminal region for ~200 μm before branching and entering the ultraterminal region (Figure 7A and Video S10). Within the terminal region, the cellular architecture remained simple and consistent. There, the Aβ RA-LTMR axon was ellipsoid (1.5 μm × 4.5 μm) with its major axis aligned with the longitudinal cleft (Figure 7B), whose orientation was maintained throughout the terminal region. The multi-layered wrapping of the inner core region was established by ~73 lamellar cells whose cell bodies were situated at the inner/outer core boundary (Figure S7A). The thin and densely packed lamellar cell processes emerging from the 73 lamellar cells precluded their complete reconstruction; however, we used *ROSA26-Confetti*, a stochastic, multicolor Cre-dependent fluorescent mouse reporter line, with a *Plp1-CreER* mouse to reveal the intermingled nature of lamellar cell processes within the Pacinian corpuscle (Figure S7B). Furthermore, we reconstructed a subset of lamellar processes originating from two distinct lamellar cells over a small portion of the terminal region within the FIB-SEM volume. Within this 5 μm portion of terminal region, we observed a handful of processes that emerged from the two lamellar cell bodies and established intermingled layers spanning the inner core region (Figure S7C). Together, these results reveal a blending of lamellar cell processes analogous to that observed within the Meissner corpuscle (Figure 6C). Intermittent gaps in lamellar cell coverage formed along the axon at the vertices of the major axis leaving the portion of axon membrane closest to the two longitudinal clefts exposed. As with the Aβ RA-LTMRs in hairy and glabrous skin, an extensive array of axon protrusions emerged from the central axon at these gaps and extended into the collagen matrix of the cleft (Figure 7B). The structure of these axon protrusions was more complex than the Aβ RA-LTMRs of the hair follicle or Meissner

Author Manuscript Author Manuscript Author Manuscript Author Manuscript

corpuscle, resembling a tree with a trunk-like base from which numerous protrusions extended like branches. The base of these protrusions was often structurally supported by a dense, local collagen network that encircled the structure and disintegrated as the protrusions extended from the central axon and branched (Figure S7D). Because of the large size of the corpuscle and the density of protrusions within it, we characterized the protrusion density and terminal structure across four small regions of the volume and used these measurements to estimate the total number of protrusions across the corpuscle. We estimate there are ~3,124 protrusions within the terminal region occurring at a density of 18.6 protrusions/μm of axon. We also estimate that ~57.9% (1,809/3,124) of these protrusions terminated by contacting lamellar cell processes in the inner core (Figure 7D), revealing a conserved structural motif analogous to the Aβ RA-LTMR lanceolate ending and Meissner corpuscle.

As the Pacinian's Aβ RA-LTMR axon transitioned from the terminal to ultraterminal region, it branched and its structure became far more complicated. Within the ~60 μm long ultraterminal region, which included 123 μm of axon, the axon expanded up to 12 μm in diameter and contained a remarkably high density of mitochondria (Figure 7C). Accompanying the dissolution of the lamellar cell cleft was the emergence of axon protrusions of greater prevalence and structural complexity at many points along the circumference of the axon. The density of axon protrusions in the Pacinian's ultraterminal region was estimated to be twice that of the terminal region, with 36.4 protrusions/μm of axon (estimated total = 4,470 protrusions). Across the two sampled regions of axon within the ultraterminal region, we found that 52.3% of protrusions terminated by contacting lamellar cell processes, suggesting that ~2,339 protrusions within the ultraterminal region likely form intimate contacts with lamellar cells (Figure 7D and Video S11). Some of the terminals of the longer and more elaborate protrusions were encased by cells at the edge of the inner core or extended beyond the inner core to contact the innermost edge of the cells forming the outer core (Figure 7C). The dense arrangement of axon protrusions within the ultraterminal region and their complex structure and reach across the inner and outer core boundary may impart elastic properties to the axon that facilitate its sensitivity to high frequency pressure transients and vibration across the entire corpuscle structure.

Comparison of axon protrusions across end organ structures

To better appreciate the quantitative form of these axon protrusions that are a conserved ultrastructural feature across the highly sensitive Aβ LTMRs with rapidly adapting responses (Figure 8A, reconstructions are displayed on the same scale), we performed a morphometric analysis on a subset of axon protrusions along the Aβ LTMR sensory axons of each end organ type, including the lanceolate endings of the guard hair, the Ret^+ and $TrkB^+$ axons of the dual-innervated Meissner corpuscle, and the sensory axon of the Pacinian corpuscle volume (Figure S8A). In general, the length of protrusions along the lanceolate endings and within the ultraterminal region of the Pacinian corpuscle were longer and the surface area of lanceolate ending protrusions was larger than those of the other sensory axons (Figures S8B and S8C); however, the functional significance of these small differences is unclear. In contrast, the notably high protrusion density and complex branching patterns of the Pacinian corpuscle axonal protrusions (Figures S8D and S8E) suggest that the spatial compactness of

Author Manuscript Author Manuscript Author Manuscript Author Manuscript

these ultrastructures may contribute to the unique high-frequency vibration sensitivity of this end organ structure.

Axon protrusions form cell junctions with non-neuronal cells across the three end organs

Across the three Aβ RA-LTMR end organs, we found that axon protrusions formed intimate associations with neighboring lamella or TSC processes, raising the possibility of physical contact points that tether the sensory axons to non-neuronal cells across the structure of each end organ. To further assess the ultrastructural nature of these intimate associations between axon protrusions and neighboring cells, we prepared high resolution TEM samples of each end organ using tannic acid, which enhances visualization of extracellular matrix components and identification of intercellular junctional complexes, such as adherens junctions.[21] Across the three end organs, we observed an abundance of fine filament-like structures and cytoplasmic densities that bridged the 15–20 nm gap between the membranes of sensory axons and their associated non-neuronal cells. These structures, which appeared structurally similar to adherens junctions, formed along the main body of the axon and neighboring TSC or lamellar cells, as has been observed previously in the hair follicles of rats,[65,66] and on the axon protrusions at sites of contact with non-neuronal cells (Figure 8B). Thus, axon protrusions not only greatly expand the axon surface area and allow for more expansive localization of Piezo2 across the sensory end organ, they also anchor the sensory axon to non-neighboring cell processes via cell-cell junctions, which physically integrate the sensory axon into the end organ microenvironment.

DISCUSSION

Our high-resolution reconstructions of the hair follicle lanceolate complex, Meissner corpuscle, and Pacinian corpuscle, and our analysis of their ultrastructural features and their subcellular distribution of Piezo2, reveal a unified model to explain Aβ RA-LTMR responsiveness and entrainment to dynamic stimuli across the morphologically dissimilar end organs of touch. We propose that, like the hooks of Velcro or the burrs on the burdock plant, the elaborate protrusions of Aβ RA-LTMR axons (Figure 8A) and their capacity to form adherens junctions with non-neuronal cells serve to fasten or anchor the sensory axon to numerous, distant locations and extend the reach of axonal Piezo2 across the end organ structure. This conserved ultrastructural feature allows deflection of hair or indentation or vibration of skin to stretch the axon membrane across hundreds to thousands of locations within an individual end organ structure, leading to gating of axonal Piezo2 and neuronal excitation (Figure 8C).

We found that Piezo2 localization in all three Aβ RA-LTMRs is restricted to terminal axons embedded within their respective end organs. The restricted localization of Piezo2 to the sensory axons and the lack of light-touch responses in Piezo2 knock-out animals,[26,27,29,30] but not in *Dhh-Cre; Piezo2*$^{f/f}$ mice (Figures 2A–E), emphasizes the indispensable, cell-autonomous role of axonal Piezo2 in light touch; however, it remains possible that TSCs and lamellar cells express other mechanosensitive ion channels that modulate the tactile responses of Aβ RA-LTMRs. By reconstructing the end organ-innervating regions of axons containing Piezo2, we were able to characterize ultrastructural features unique to Aβ RA-

Author Manuscript Author Manuscript Author Manuscript Author Manuscript

LTMRs that may underlie their responsivity to dynamic stimuli. Despite the dissimilar microenvironments in which each Aβ RA-LTMR resides—neighboring a hair follicle, associated with bone, or wedged within a dermal papilla near the surface of glabrous skin—we observed remarkable ultrastructural homology across these three end organ structures. We found an abundance of axon protrusions to be a unique structural feature conserved across the Aβ RA-LTMRs within each end organ structure. Our observation that a large portion of the Aβ RA-LTMR axon protrusions contact non-neuronal cells and form cell-cell junctions suggests a tether-like function for these axonal structures first described over 50 years ago.[23,44–47] Although our FIB-SEM volume did not contain slowly adapting (SA) Aβ LTMRs, which form the crown-like touch dome, previous ultrastructural analysis suggests that the terminal nerve plate of Aβ SA-LTMRs is smooth and lacks any discernable protrusion-like structures.[20] Collectively, this suggests these axon protrusions and their tethers are ultrastructural features reserved for the most sensitive sensory neurons involved in detecting dynamic touch.

Mechanical cell-cell coupling stabilizes tissue architecture and enables cells to sense and respond to tensile and shear forces in their microenvironment.[67] The abundance of junctions along the Piezo2-enriched region of Aβ sensory axons suggests that they play a central role in transforming mechanical stress across the end organ structure into sensory axon membrane strain, resulting in Piezo2 activation. We observed adherens junctions joining the main body of the sensory axon to its most proximate TSC or lamellar processes as well as at contact points between axon protrusions and more distant non-neuronal cell processes. We speculate that these junctions along the axon body and protrusions act as anchor points that enhance the transmission of forces from more peripheral portions of the end organ to the central axon body, helping to explain the low-threshold responses of Aβ RA-LTMRs. We found that in the hair follicle, ~50% of protrusions from Aβ RA-LTMRs surrounding the guard hair extend beyond the longitudinal collagen network and enter the circumferential collagen matrix. Of the 880 protrusions that bridged these perpendicular collagen networks, over half form intimate contacts with cell processes embedded within the circumferential collagen matrix. These contacts anchor the protrusions within the circumferential collagen matrix, which may result in the unique sensitivity of the sensory axons to the shear, compressive, tensile, and torsional stress that occurs during hair deflection or nearby skin indentation (Figure 8C). A majority of these contacts in the circumferential collagen network are made with a previously unidentified cell type, which we term the circumferential support cell or CSC, revealing a novel cellular component of lanceolate ending structure and possibly function. Previous work has shown that N-cadherin localizes to the cell-cell junctions that form between the sensory axons and adjacent TSCs of rat hair follicles.[66] Whether N-cadherin is required for adherens junctions that form along the protrusions and within the circumferential collagen matrix described here, and the role of N-cadherin in mechanotransduction of Aβ RA-LTMRs remain to be explored.

In the Meissner corpuscle and Pacinian corpuscle, we speculate that tactile forces induce maximal bending and strain along the axon protrusions extending into the collagen network (Figure 8C). These forces may be effectively transferred to the main body of the axon as a result of the cell-cell junctions formed between the extensive array of axon protrusions and distant lamellar cell processes. In the Meissner corpuscle, we found that the more

Author Manuscript Author Manuscript Author Manuscript Author Manuscript

sensitive TrkB$^+$ Aβ RA-LTMR exhibited twice the number of protrusions and four times the protrusion density compared to the less sensitive Ret$^+$ sensory axon. While an equal proportion of protrusions from the two sensory neuron types formed contacts with lamellar cells within the corpuscle, we suspect that the higher density of protrusions of the TrkB$^+$ axon render it more sensitive to dynamic, tactile stimulation. Our reconstruction of the Pacinian corpuscle, and specifically of the ultraterminal region, revealed the densest array of axon protrusions among the Aβ RA-LTMRs (Figures S8D and S8E). The Pacinian corpuscle is unique among LTMR end organs in its high-pass frequency tuning. We speculate that the extensive axon protrusions and their elaborate lamellar cell contacts, together with the unique resonance properties of this end organ and the remarkably high density of axonal mitochondria underlie the Pacinian Aβ RA-LTMR's capacity to entrain to high frequency mechanical stimuli.

Collectively, our high-resolution Aβ RA-LTMR end organ architecture analyses show axon protrusions and their intimate contacts with resident, non-neuronal cells to be a common ultrastructural motif that we propose underlies the low force threshold activation of Aβ RA-LTMR axon membrane-bound Piezo2. We observed a similar motif in lanceolate endings surrounding non-guard hairs, which are predominantly innervated by comparably sensitive low-threshold Aδ- and C-LTMR sensory neurons[8] that also respond to dynamic touch, suggesting these axon protrusions and their non-neuronal contacts are a conserved feature of ultrasensitive low-threshold mechanoreceptors that innervate specialized end organ structures involved in the detection of dynamic, light touch. Furthermore, given the structural homology of hair follicle lanceolate endings, Meissner corpuscles, and Pacinian corpuscles across species, we speculate that Aβ RA-LTMR end organ axon protrusions and the adherens junctions they form with surrounding support cells represents a basic functional unit of mechanotransduction in humans as well.

STAR METHODS

RESOURCE AVAILABILITY

Lead Contact—Further information and requests for resources and reagents should be directed to and will be fulfilled by the lead contact, David Ginty (david_ginty@hms.harvard.edu).

Material Availability—The *Piezo2$^{smFP\text{-}FLAG}$* mouse line is available upon request.

Data and Code Availability—All data reported in this study and code used for analysis will be shared by the lead contact upon request. All raw-aligned and segmented FIB-SEM volumes generated for this study will be available through Janelia's OpenOrganelle data portal upon publication.

EXPERIMENTAL MODEL AND SUBJECT DETAILS

Mice used in this study were maintained on mixed C57Bl/6J and CD1 backgrounds, except for mice used for the hair follicle (MH200121-B2K) and two Meissner Corpuscle FIB-SEM samples (200913FPT and 200913FPT2), which were pure C57BL/6J, and included both

Author Manuscript Author Manuscript Author Manuscript Author Manuscript

males and females. The *Piezo2*$^{smFP\text{-}FLAG}$ knock-in allele was generated at the Janelia Campus Research Gene Targeting and Transgenic Facility. The knock-in targeting construct was produced using recombineering techniques and traditional molecular cloning. A 5,197 bp of genomic DNA fragment containing exons 53 and 54 of the *Piezo2* gene was retrieved from BAC clone RP24–130D5. The *smFP-FLAG* gene was fused to Exon 54 followed by an frt-NeoR-frt cassette for ES cell selection. The homologous arms of the construct were 3,542 bp and 2,075 bp respectively. To facilitate ES cell targeting Crispr/cas9 system was used. gRNA was invitro transcribed using MEGA shortscript T7 kit (Life Tech Corp AM1354). The template was PCR amplified using primers:

Forward 5'-
CCTTAATACGACTCACTATAGGCAAACTGATCACTTAAGACCTGGGTTTTAGAGCT
AGAAATAGC -3'

Reverse 5'-
AAAAGCACCGACTCGGTGCCACTTTTTCAAGTTGATAACGGACTAGCCTTATTTTA
ACTTGCTATTTCTAGCTCTAAAAC -3'

The gRNA was tested *in vitro* before being used for ES cell targeting. The test was carried out in a reaction of NEB 3.1 buffer 1ul, DNA template 120 ng, gRNA 40 ng, Cas9 160 ng in a total volume of 10 ul. The reaction mix was incubated at 37C for 2 hours. 0.5 ul proteinase K (20ug/ul) was then added and incubated at 57C for 30 min.

The targeting vector, cas9 protein (Fisher Scientific A36499 TRUECUT CAS9 PROTEIN V2) and the gRNA with concentrations of 10 ug, 3.75 ug and 1 ug respectively in total volume of 100 µl were co-electroporated into 1 million of G1 ES cells, which were derived from F1 hybrid blastocyst of 129S6 × C57BL/6J. Seventy-four G418 resistant ES colonies were isolated and screened by nested PCR using primers outside the construct paired with primers inside the construct. The primers used for ES cell screening were as following:

5' arm forward primers: Sptbn1 Scr F1 (5'- CGCTCACTAGAGCAAAGTTG -3') and Sptbn1 Scr F2 (5'- TAGGGTTCCTAGTAGGATCC -3'). Reverse primers: Cre scr R1 (5'- GAGGGACCTAATAACTTCGT -3') and Cre scr R2 (5'- ATGATCGGAATTGGGCTGCA -3').

3' arm forward primers: mMapple scr F1 (5'- CCATAGGATCGAGATCCTGT -3') and mMapple scr F2, (5'- GACTACAACAAGGTCAAGCTGT -3'); Reverse primers: Sptbn1 Scr R1 (5'- CAGAGCAGCAGTTCTGACTT -3') and Sptbn1 Scr 3R2 (5'- GACCCCAGAGATCTAATTCC -3');

Thirty-eight of 48 ES cell clones screened contained both arms. Three of them were used for making chimeric mice. Chimeric mice were generated by aggregating the ES cells with 8-cell embryos of CD-1 strain. After achieving successful germline transmission of the *Piezo2*$^{smFP\text{-}FLAG}$ gene in one strain, the frt-NeoR-frt cassette was excised. Proper insertion of the gene into the Piezo2 locus was confirmed with loss of the wild-type Piezo2 gene in a mouse homozygous for the knock-in allele using the following primers:

Author Manuscript Author Manuscript Author Manuscript Author Manuscript

Forward5’ Piezo2-Exon54: TGGAACTGGAGGAAGACCTCTACG

Reverse5’ Piezo2-smFP-FLAG: GAACAGCTCCTCGCCTTTCG

Reverse5’ Piezo2–3’UTR: CCCTGATTTCAGAGACATGGGAGT

Mice with two copies of *Piezo2*$^{smFP\text{-}FLAG}$ appeared phenotypically similar to heterozygote and wild-type littermate animals. We observed no difference in distance traveled in open field or time to cross a balance beam between genetic groups (Figure S1D and S1E), suggesting that smFLAG insertion does not have a profound impact on Piezo2’s function. However, we did not perform single-channel recordings to assess electrophysiological differences in the tagged compared to the untagged channel.

To achieve specific labeling of sensory neuron subtypes, CreER driver lines were induced by administering tamoxifen dissolved in sunflower seed oil via intraperitoneal (I.P.) injection. Tamoxifen (MilliporeSigma) was dissolved in ethanol (MilliporeSigma) and then mixed with an equal volume of sunflower seed oil (MilliporeSigma). The mixture was vortexed, and ethanol was then removed under vacuum. The dosage for tamoxifen was as follows: for *Plp1*^{CreER}, mice received an I.P. injection of 1 mg of tamoxifen for 5 days (P15-P19); for *TrkB*^{CreER}, mice received an I.P. injection of 0.5 mg at P4; for *TrkC*^{CreER}, mice received an I.P. injection of 0.5 mg of tamoxifen at P5.

Plp1^{EGFP} (JAX 033357)[68] and *Plp1*^{CreER} (JAX 005975)[69] were used to label Schwann cells. *ROSA26LSL-Matrix-dAPEX2* (JAX 032765) and *ROSA26FSF-Matrix-dAPEX2* (JAX 032766) were used for genetic EM labeling.[60] *TrkC*^{CreER} (JAX 030291) was used to label Aβ field LTMRs.[2] *CGRP*^{FlpE} was used to label Aδ HTMRs.[70] *Cav1*$^{-/-}$ (JAX 007083) was used to ablate caveolae.[71] *TrkB*^{CreER} (JAX 027214)[72] together with *Advillin*^{FlpO} [70] and *ROSA26*$^{FSF\text{-}LSL\text{-}tdTomato}$ (JAX 021875)[73] was used to selectively label Meissner Aβ RA-LTMRs. *NPY2RGFP* (GENSAT 011016-UCD) was used to label hairy Aβ RA-LTMRs. *ROSA26*$^{CAG\text{-}Brainbow2.1}$ (JAX 017492) was used to visualize different lamellar cells in the Pacinian corpuscle.[74,75] *Cdx2*^{Cre} was used to delete Piezo2 in the sensory neurons and peripheral Schwann cells.[76] *Piezo2*$^{-/-}$ and *Piezo2*$^{fl/fl}$ were used to delete Piezo2 in a Cre-independent[77] and dependent manner.[36] *Dhh*^{Cre} was used to delete Piezo2 in peripheral Schwann cells (JAX 012929).[78] Mice were handled and housed in standard cages in accordance with the Harvard Medical School and IACUC guidelines.

METHODS DETAILS

Immunofluorescent staining—Tissue was isolated from P20 or older mice that were euthanized with isoflurane or sedated using a ketamine/xylazine mixture. Forepaw digit tips were cut to isolate tissue containing Meissner corpuscles. The back was treated with Nair to remove all hair and a large section of skin was cut. The fat on the underside of the hairy skin was removed to improve antibody penetration. Pacinian corpuscles were isolated from the periosteum membrane from the fibula of the mouse. The entire periosteum was isolated for whole mount staining. For staining of the Pacinian with cyrosections, *Plp1*^{EGFP} mice were used to visualize and isolate Pacinian corpuscles in the periosteum membrane. Tissues were drop fixed in either 1% paraformaldehyde (PFA) in phosphate-buffered saline (PBS)

Author Manuscript Author Manuscript Author Manuscript Author Manuscript

for 1–2 hours at 4°C (for more sensitive antibodies) or Zamboni's fixation buffer for 24 hours at 4°C. Following fixation, all tissues were rinsed in PBS and processed for 25 μm sections or whole mount staining as previously described.[3] For Figure S6F, forepaw digit tips were sectioned at 200 μm and processed for whole mount staining. For each section, the proportion of Meissner corpuscles (labeled by S100B) that were innervated by a TrkB afferent (labeled by tdTomato) was calculated.

Primary antibodies were goat anti-mCherry (Sicgen, cat. no. AB0040–200, 1:500), chicken anti-GFP (Aves Lab, cat. no. GFP-1020, 1:500), rabbit anti-GFP (Invitrogen, cat. no. A-11122, 1:500), goat anti-GFP (US Biological, cat. no. G8965–01E, 1:500–1:1000), rabbit anti-S100 beta (ProteinTech, cat. no. 15146–1-AP, 1:300), rabbit anti-TUJ1 (Biolegend, cat. no. 802001, 1:500), chicken anti-neurofilament heavy chain (Aves, SKU: NFH, 1:300–1:500), rabbit anti-CGRP (Immunostar, cat. no. 24112, 1:375), and guinea pig anti-FLAG (1:500).[79] The same laser settings and contrast/brightness adjustments were made in Figures 1B and S1G to compare FLAG levels in *Piezo2*$^{smFP\text{-}FLAG}$ animals and littermate controls.

Electron microscopy sample preparation—Skin/tissue regions enriched for Meissner corpuscles, hair follicles, and Pacinian corpuscles were dissected as follows for electron microscopy (EM) sample preparations. The forepaw digit tips were dissected to isolate Meissner corpuscles. For hairy skin samples that focused on the ultrastructure of an isolated guard hair, all hairs except the guard hair were trimmed in a small piece of back hairy skin, allowing us to track the location of a guard hair follicle within the sample. Non-guard hairs were identified for analysis in Figure S5D based on their smaller follicle size and ultrastructural features. Pacinian corpuscles were isolated and dissected from the periosteum membrane surrounding the fibula using the fluorescent marker Plp1^{EGFP}. Tissue samples containing forepaw digit tips, back hairy skin, and Pacinian corpuscles were immersed in a glutaraldehyde/formaldehyde fixative for 1 hour at room temperature, further dissected to remove muscle and fat, and subsequently fixed overnight at 4 °C. Sample preparation was done as previously described.[60] Ultrathin sections were cut at 50–70 nm and imaged using a JEOL 1200EX transmission electron microscope at 80 kV accelerating voltage. Images were cropped and adjusted to enhance contrast using Fiji/ImageJ. For tannic acid treatment, samples were incubated in cacodylate buffer containing 1% low molecular weight tannic acid for 30 min (Electron Microscopy Sciences) between the osmication step and the uranyl acetate step, with washes preceding and following this treatment. Ultra-thin sections were then stained with uranyl acetate and lead citrate. All single section TEM images presented in the paper were pseudo-colored by hand.

FIB-SEM sample preparation—Skin/tissue regions enriched for Meissner corpuscles, hair follicles, and Pacinian corpuscles were dissected as described above. Four durcupan embedded mouse end organ samples: one hair follicle sample (MH200121-B2K), two Meissner Corpuscle samples (200913FPT and 200913FPT2), and one Pacinian Corpuscle sample (Pacinian2A) were prepared for FIB-SEM as described previously.[80] Specifically, each sample was first mounted to the top of a 1 mm copper post, which was in contact with the metal-stained sample for belter charge dissipation, as previously described.[53] The vertical sample posts were each trimmed to a small block containing the Region of Interest

Author Manuscript Author Manuscript Author Manuscript Author Manuscript

(ROI) with a width perpendicular to the ion beam, and a depth in the direction of the ion beam. The block sizes were 105 × 100 μm^2, 90 × 70 μm^2, and 85 × 75 μm^2, and 140 × 120 μm^2 for MH200121-B2K, 200913FPT, 200913FPT2, and Pacinian2A respectively. The trimming was guided by X-ray tomography data obtained by a Zeiss Versa XRM-510 and optical inspection under a Leica UC7 ultramicrotome. Thin layers of conductive material of 10-nm gold followed by 100-nm carbon were coated on the trimmed samples using a Gatan 682 High-Resolution Ion Beam Coater. The coating parameters were 6 keV, 200 nA on both argon gas plasma sources, and 10 rpm sample rotation with 45-degree tilt.

FIB-SEM 3D large volume imaging—These four FIB-SEM prepared samples, MH200121-B2K (guard hair follicle volume), 200913FPT (single innervated Meissner corpuscle), 200913FPT2 (dual innervated Meissner corpuscle) and Pacinian2A (Pacinian corpuscle) were imaged by four customized Zeiss FIB-SEM systems previously described.[53,81,82] Each block face of ROI was imaged by a 1-nA electron beam with 0.9 keV landing energy. The x-y pixel resolution was set at 6 nm. A subsequently applied focused Ga+ beam of 15 nA at 30 keV strafed across the top surface and ablated away 6 nm of the surface. The newly exposed surface was then imaged again. The hair follicle (MH200121-B2K) and Meissner Corpuscle (200913FPT and 200913FPT2) samples were imaged at 1 MHz throughout their entire volumes. The ablation – imaging cycle continued about once every three and a half minutes for five weeks to complete FIB-SEM imaging MH2001–21B2K, and about once every minute for one week to complete 200913FPT and 200913FPT2. To best balance the total acquisition duration and the image quality (signal to noise ratio) in critical sections, the Pacinian Corpuscle sample was imaged sequentially using three different SEM scanning rates of 3 MHz, 2 MHz and 1 MHz for the top (myelinated region and part of the terminal region), middle (terminal region and part of the ultraterminal region) and bottom (ultraterminal region) sections of ROI, respectively. The ablation – imaging cycle continued about once every 50 seconds for 16 days to complete the top section ROI of 55 × 60 × 185 μm^3, continued about once every 65 seconds for 9 days to complete the middle section ROI of 55 × 60 × 70 μm^3, and continued about once every 2 minutes for 13 days to complete the bottom section ROI of 55 × 60 × 60 μm^3. The entire Pacinian2A sample was FIB-SEM imaged for 38 days. Each acquired image stack formed a raw imaged volume, followed by post processing of image registration and pairwise alignment using a Scale Invariant Feature Transform (SIFT) based algorithm. The aligned stack consists of a final isotropic volume of 80 × 80 × 80 μm^3, 30 × 40 × 50 μm^3, 35 × 40 × 40 μm^3 and 55 × 60 × 291 μm^3 for MH200121-B2K, 200913FPT, 200913FPT2, and Pacinian2A respectively. The voxel size of 6 × 6 × 6 nm^3 was maintained for each sample throughout the entire volume, which can be viewed in any arbitrary orientations. 174 nm was missing in MH200121-B2K between slice 6483 and slice 6484 due to microscope issues.

Global image alignment and processing—Three slices (7597, 7598, 7962) were discarded in MH200121-B2K due to microscope issues, and adjacent slices (7596, 7599, 7961) were copied over. For global alignment, the SIFT-aligned FIB-SEM stacks were downsampled 32x to 192 nm × 192 nm × 192 nm voxel size and adjusted for contrast to reduce illumination unevenness. μCT volumes were cropped to just large enough to fully include the FIB-SEM ROI. The downsampled FIB-SEM stacks were used as moving images

Author Manuscript Author Manuscript Author Manuscript Author Manuscript

to align to μCT stacks which were fixed images using elastix.[83,84] The elastix alignment was done in a manner similar to Phelps et al. (2021)[85] (https://github.com/htem/run_elastix), where an affine alignment was followed by a B-spline elastic alignment. Mutual information (AdvancedMattesMutualInformation) was used as the main metric, and 28 grid spacing and 0 bending weight was used for B-spline alignment to avoid distortions. Corresponding points were added whenever necessary. After satisfactory alignment was achieved, the transform was inverted to allow the mapping of coordinates in the SIFT-aligned FIB-SEM space to the μCT space. In order to align images by translation alone to reduce distortion, the geometric center of each section was mapped to the μCT space, given that it is rotationally invariant and in general in a well aligned region for elastix alignment. Since the z-axes were nearly identical in direction for the SIFT-aligned FIB-SEM volume and the μCT volume, these transformed coordinates can then be used as displacement vectors to align raw image stacks.

To generate the final volumes, raw FIB-SEM images were first processed to clean up milling artifacts using Fourier transform,[53] and then contrast enhanced using CLAHE. Images were then placed using displacement vectors generated above into an aligned volume. Volumes were rotated in 3-D space to align their z-axes to major anatomical axes, such as the hair shaft, for the ease of visualization and analysis.

Automated segmentation and reconstruction—We used Segway, a segmentation pipeline previously developed for segmentation of transmission EM data[54] and later refined for X-ray and isotropic data segmentation,[86] to automatically segment the FIB-SEM datasets. Segway uses a 3D U-Net convolutional neural network (CNN) model to create an affinity map to predict a ‘connectedness’ probability of each voxel to adjacent voxels.[87] CNN models were trained using ground truth labels generated through manual segmentation of small image volumes that included the sensory axons, non-neuronal cells of interest, as well as “background” regions (e.g., “empty” areas that should be masked out for reconstruction) using webKnossos.[88] A separate CNN model was generated for each dataset using volume-specific ground truth for MH200121-B2K (guard hair follicle volume), 200913FPT2 (dual-innervated Meissner corpuscle volume), and Pacinian2A (Pacinian corpuscle volume), except for 200913FPT which used the same CNN model as 200913FPT2 due to their homology. For CNN training we used Gunpowder (https://github.com/funkey/gunpowder/) to randomly sample batches and perform data augmentation; the network architecture and training parameters are as previously described,[86] though in these models we also use long-range affinities[89] to improve prediction accuracy. After the models were trained, Daisy (https://github.com/funkelab/daisy) was used to deploy the CNN models and subsequent post-processing steps in the Segway pipeline to generate the output segmentation.

All volumes were segmented at 6 × 6 × 6 nm resolution except the Pacinian volume which was segmented at 12 × 12 × 12 nm to increase performance speed without a noticeable increase in error. To proofread and reconstruct neurons, we used MD-Seg, a merge-deferred segmentation proofreading method.[54] This method pre-agglomerates segmentation fragments only in a local block instead of across the entire volume to avoid catastrophic merge error propagations that often occur in large volumes. Inter-block merge decisions are computed and accessible to the proofreader during the reconstruction in the

Author Manuscript Author Manuscript Author Manuscript Author Manuscript

user interface using a hotkey. This pre-agglomeration threshold was 0.5 (out of a range from 0.0 to 1.0) for all volumes except for Pacinian2A which was 0.9 because only the axon was constructed and to minimize proofreading time of split errors.

To reconstruct the sensory neurons and non-neuronal cells of interest within our FIB-SEM volumes, we first identified the cells to be reconstructed based on their stereotypical morphological characteristics and selected a cell fragment that was contained within a single block. Using the hotkey, mergeable fragments in adjacent blocks were added to the single block from all sides. Sequential use of the hotkey enabled the proofreader to 'grow' the cell by continually adding computed merge fragments at the boundaries of the growing cell. In the event of a merge error, growth from the block containing the error could be blocked and removed from the reconstruction to prevent any further growth from the merged segment.

In each volume, all myelinated Aβ sensory neuron axons were reconstructed. Also, a subset of small diameter neurons that innervated the hair follicle and Meissner corpuscle were reconstructed. Additional small diameter axons in the circumferential collagen were seen but their restricted innervation pattern was dissimilar to the anatomical characteristics of the Aδ circ-HTMR. The terminal Schwann cells that associated with the lanceolate endings in the MH200121-B2K (guard hair follicle volume) and the lamellar cells that associated with the Aβ sensory axons in the 200913FPT2 (dual-innervated Meissner corpuscle volume) were reconstructed to visualize the intimate interactions between the non-neuronal cells of the end organs and the Aβ sensory axons. Additionally, we reconstructed a subset of the circumferential terminal Schwann cells that associated with the Aβ field LTMRs (this subset represents the majority of circumferential terminal Schwann cells in the volume) and a subset of previously uncharacterized circumferential support cells (CSCs) because of their numerous contacts with the protrusions of the Aβ sensory axons of the hair follicle. Based on structural homology, we estimate there to be roughly 17 total CSCs with cell bodies that reside in the circumferential collagen matrix on the same horizontal plane as the lanceolate endings. Additional non-neuronal cells were observed in the volume but were not reconstructed. All single sections from FIB-SEM volumes presented in the paper are pseudo-colored by the trained networks.

Immuno-electron microscopy sample preparation—Skin regions enriched for Meissner corpuscles, hair follicles, and Pacinian corpuscles were isolated from *Piezo2*$^{smFP\text{-}FLAG}$ mice or littermate controls. The *Plp1*^{EGFP} allele was also present in all mice to aid sample preparation. Forepaw digit tips were isolated as described above. For back hairy skin, all hairs were trimmed short, and a rectangular piece of skin (~1 mm x 2 mm) was dissected with the rostral/caudal axis oriented along the long axis of the sample. Pacinian corpuscles were isolated as described above. Samples were drop fixed in 4% PFA in 0.1 M phosphate buffer (PB) for 2 hours at room temperature. Samples were micro-dissected 1 hour into fixation to remove access fat and muscle and returned to fix for the remainder of the 2 hours.

After samples were washed in 0.1 M PB, they were cryoprotected in 30% sucrose in 0.1 M PB. Samples were then embedded in Neg-50 Frozen Section Medium (VWR, cat. no. 21008–918). Immediately after the samples were embedded, they were cryosectioned into

Author Manuscript Author Manuscript Author Manuscript Author Manuscript

50 μm sections and placed into chilled 0.1 M PB. Plp1^{EGFP} mice were used to visualize and isolate sections with end organ structures. Sections were then incubated in 50 mM glycine in 0.1 M PB for 30 minutes. After aldehyde quenching, sections were blocked in 10% normal goat serum (Vector labs, cat. no. S-1000), 0.5% fish gelatin (Sigma, cat. no. G7041), and 0.05% Triton X-100 in 0.1 M PB for 2 hours at room temperature. Sections were then incubated with primary antibody in a modified blocking solution—10% normal goat serum, 0.5% fish gelatin, 1:100 guinea pig anti-FLAG[79] in 0.1 M PB—for 24 hours at room temperature under gentle agitation. After a series of washes in 0.1 M PB, sections were incubated overnight with species-specific gold-labeled secondary antibody in a modified blocking solution—10% normal goat serum, 0.5% fish gelatin, 1:50 Nanogold-Fab' goat anti-guinea pig IgG (Nanoprobes, cat. no. 2055) in 0.1 M PB. After washes in 0.1 M PB, sections were post-fixed with 1% glutaraldehyde for 10 minutes before being thoroughly rinsed with dH2O.

To reveal gold labeling, sections were incubated with HQ Silver Enhancement (Nanoprobes, cat. no. 2012) for 8 minutes under gentle agitation. The enhancement reaction was quenched by the addition and subsequent rinses with dH2O. Following silver staining, samples were stained with 1% osmium tetroxide in 0.1M PB for 30 minutes and subsequently 1% uranyl acetate in 0.05 M maleate buffer overnight at 4°C. Sections were then dehydrated with serial ethanol and propylene oxide (VWR, cat. no. 20411) dilutions before infiltration and embedding in an epoxy resin (LX-112, Ladd Research) mix and cured at 60°C for 48–72 hours. Ultrathin sections were cut at 50–70 nm and imaged using a JEOL 1200EX transmission electron microscope at 80 kV accelerating voltage. Images were cropped and adjusted to enhance contrast using Fiji/ImageJ.

Quantification of Immuno-electron Microscopy Signal—To quantify immuno-electron microscopy signal as enhanced by silver staining, the "Analyze Particles" function of Fiji/ImageJ was applied to 4–6 representative thresholded images selected for each animal. After properly setting the pixel-to-micron scale, images were uniformly cropped to exclude the attached metadata and smoothed to limit any static-like background signal. In all tissue types, the axon membrane was carefully traced in a freehand selection to include any overlying puncta and saved as a region of interest (ROI). The same was done for the surrounding lamellar cells in the lanceolate complexes and Meissner corpuscles, however, the increased lamellar complexity and decreased ultrastructural resolution prevented such an analysis in the Pacinian corpuscles. These ROIs were shrunk by 80 nanometers, and the resulting ROIs were considered to be the "internal" ROIs of the lamellar or axon profiles, and the 80 nanometer-thick, nonoverlapping region between the external and internal ROIs was considered to be the membrane. In the analysis of all images, the membrane thickness was maintained as 80 nanometers to include the majority of large, membrane-associated puncta without including clearly internal puncta. The extracellular space of lanceolate and Meissner images was isolated by selecting the inverse of the axon, lamellar cells, and any other cells. Due to the increased lamellar cell complexity, density and decreased ultrastructural resolution of sections taken from the Pacinian corpuscle, the entire image, excluding the axon membrane and internal axon was categorized as "other."

Author Manuscript Author Manuscript Author Manuscript Author Manuscript

With ROIs made for analysis, the image was then thresholded with a minimum of 0 and maximum of 90, such that only the dark puncta were visible. The maximum of 90 was chosen, as any lower reduced the size of the puncta, and any higher included non-puncta relatively dark components of the image or background. Some images required adjustment of exposure or threshold to ensure that puncta were accurately captured. This thresholding process occasionally left dark spots of tears or particulates that were manually excluded from analyzed ROIs. The "Analyze Particles" function was then used on the ROIs corresponding to the axon membrane, internal axon, lamellar membrane, internal lamellar, extracellular space, and, with the Pacinian images, non-axonal space with a minimum size of 0.1 square nanometers to exclude any remaining static-like noise. For plotting, we used the automatically generated output average for puncta size and percent of ROI occupied by puncta (puncta area divided by ROI area).

Quantification of lamellar cell wrappings—Six and nine imaging planes distributed through the single-innervated Meissner corpuscle and the dual-innervated Meissner corpuscle, respectively, were selected for lamellar cell wrapping analysis. A line was drawn through the center of each Aβ sensory axon profile for each imaging plane. The line extended to the boundary of lamellar cell processes believed to associate with each individual axon profile. The number of lamellar cell processes crossing that line were used to determine the number of lamellar cell processes wrapping that particular axon profile. This analysis is similar to previously described work.[3]

Protrusion ending quantification—To characterize the terminal properties of axon protrusions, the final 50% of a protrusion was examined to assess whether it formed a contact (<30 nm of space between membranes) with a neighboring cell. In the hair follicle volume, protrusions along the Aβ RA-LTMRs were categorized as terminating either in the local longitudinal collagen matrix or in the more distal circumferential collagen network. If a protrusion extended into the circumferential collagen network and came within ~30 nm of a terminal Schwann cell that was also within the circumferential collagen, then it was counted as a contact with a cell in the circumferential collagen. Protrusions were also counted along the Aβ field-LTMRs. Small bumps along the sensory axons were not counted as protrusions. The same metrics were used to characterize the axon protrusions within both Meissner corpuscle FIB-SEM volumes. Because of the large size of the Pacinian corpuscle and the density of protrusions, we counted the number of protrusions and characterized their terminal endings in representative regions of the corpuscle and used that quantification to estimate the total number of protrusions and their terminal structures within the terminal and ultraterminal region. Two different regions in the terminal and ultraterminal region were selected to characterize protrusions to ensure we captured as much heterogeneity in protrusion density and terminal structure as possible across this large structure.

Morphometric analysis of axon protrusions—We analyzed the morphometric properties (length and surface area) using the NeuroMorph 3D analysis toolkit[90,91] in Blender for a subset of representative protrusions distal to the branch point for each particular protrusion across each end organ type (https://neuromorph.epfl.ch/). The 3D meshes of the Aβ LTMR lanceolate endings of our guard hair follicle volume, Ret^+ and

Author Manuscript Author Manuscript Author Manuscript Author Manuscript

TrkB$^+$ axons of the dual-innervated Meissner corpuscle volume, and the single Aβ LTMR sensory axon of the Pacinian corpuscle volume were imported into Blender. In Blender, meshes were remeshed with the 'smooth' setting at an octree depth of 12. The meshes were then decimated to a value of 0.01 for the hair follicle and Meissner corpuscle volume and 0.2 for the Pacinian corpuscle volume, resulting in meshes with reduced face counts with minimal shape changes. NeuroMorph was then used to calculate the length of protrusions by selecting a vertex at the tip of the protrusion and the base (where axon protrusion merges with axon body or branches) and using the 'shortest distance along mesh' function. To calculate surface area, all faces along the protrusion (from tip to base) were selected and the measurements tool was used to calculate surface area.

***In vivo* DRG electrophysiology—**Juxtacellular recordings were made from DRG neurons *in vivo*. Mice of both sexes were anesthetized with urethane (1.5 g/kg). An incision was made over the lumbar spine and scalp. A headplate was fixed to the skull using cyanoacrylate adhesive. The muscle overlying the DCN was removed, and the dorsal aspect of the C1 vertebrae was removed. The L4 DRG was exposed and two custom made spinal clamps fixed the spine in place. A platinum-iridium bipolar stimulus electrode (FHC) was lowered into the caudal DCN or C1 DC. A glass electrode (borosilicate, 1–2 MO) filled with saline was lowered into the DRG. Electrical stimuli (25–300 μA, 0.2 ms duration) were delivered to the DCN/DC at 0.5–1 Hz while searching for a unit. Once an antidromically activated unit was isolated, the receptive field was determined by brushing the hindlimb and thigh. If no receptive field could be identified, a series of stimuli were systematically delivered to the hindpaw and thigh to search for activation. Once the receptive field was located, one of three stimuli were delivered. Air puffs (5 PSI from a 20 gauge needle, 1–3 mm from the hair) were used for hairy skin. For glabrous skin, a custom-built mechanical stimulator delivered static indentations (0–25 mN) using a 0.2 mm diameter probe tip. In some cases, vibration (10–1000 Hz, 0–25 mN) was delivered using the same stimulator. Signals were amplified using a Multiclamp 700A/B and acquired using a Digidata 1550A/B using Clampex 10/11 software. For Aβ RA-LTMRs shown in Figure S1A, cells were visualized under a microscope in BAC-transgenic *NPY2R-GFP* mice[8] and large glass electrodes (20–30 μm tip diameter) were used to perform targeted recordings as previously described.[3] Force indentations (0.5 s duration 1–75 mN intensity) and sine vibrations of varying frequency and intensity were used to characterize the response properties of five NPY2RGFP$^+$ cells isolated from four animals. Similar responses were observed for all isolated cells.

DRG electrophysiology analysis—Units that were antidromically identified from DCN/DC stimulation were sorted into categories based on their response properties. Units that had their mechanical receptive field on hairy skin and were activated by movement of hairs were classified as either 'guard hair Aβ RA-LTMR' or 'limb hair Aβ RA-LTMR', depending on their responses to deflection of different hair types. Units that had receptive fields on glabrous skin were classified as either 'Meissner Aβ RA-LTMR' or 'Aβ SA-LTMR' depending on their adaptation properties. Units that did not have a cutaneous receptive field but could become phase-locked to high frequency vibration (>300 Hz) were classified as 'Pacinian Aβ RA-LTMR'. Units were also detected that specifically responded

Author Manuscript Author Manuscript Author Manuscript Author Manuscript

to mechanical stimulation of the toenail and were classified as 'toenail Aβ RA-LTMR'. These units also phase-locked to high frequency vibration (300 Hz). Units that lacked a specific cutaneous receptive field, but responded strongly to bending of the toe were identified as 'proprioceptor'. If units in any animal did not respond to air puff, brush, or strong vibration delivered to the thigh, trunk, or hindlimb, the units were classified as 'insensitive'. In *Cdx2*^{Cre}; *Piezo*$^{fl/fl}$ animals receptive fields were not discernable by brushing. Air puffs and brushes were delivered systematically across the hindlimb and thigh. The hindlimb was pinched if no mechanically evoked responses could be found in order to confirm that the nerve from the DRG to the periphery was not damaged. Pinching in some cases evoked firing in antidromically-identified units, but in many recordings activated units that were not activated by DCN/DC stimulation.

Open field and balance beam behavior analysis

Open Field Test: Two days prior to open field testing animals were moved to the testing room and home cage habituated to the behavior room to acclimate to room lighting, sound, odor and temperature. Animals were habituated to investigator handling by undergoing tail inking. On the third day following room habituation each animal was placed in a black matte acrylic Open field chamber (25 cm × 25 cm) and allowed to freely explore for 5 minutes. A top video recording was used to track distance traveled and generate movement trace maps of each animal.

Balance Beam Test: The balance beam was constructed of a 1 meter matte white acrylic bar with a flat 12 mm surface. The beam was mounted ~50 cm above the bench top. A black matte acrylic box was placed at each end of the beam to provide a start and end enclosure for the animal. A soft pad was stretched below the beam to serve as a soft landing surface to cushion falls. A digital USB 2.0 CMOS video camera was mounted above the balance beam to record crossings.

One hour prior to training and testing animals were habituated to behavior room to acclimate to room lighting, sound, odor and temperature and investigator handling by undergoing tail inking. To train the animals to cross freely, each animal was placed on the beam and encouraged to cross at least 3 times before returning to the home cage. If animals refuse to cross, the investigator gently touched the hindquarters to encourage forward movement. Animals habituated and trained to freely cross the beam were then tested and 4 beam crossings were video recorded. Each animal was allowed to rest for no more than 10 seconds between each crossing. The animals were then returned to their home cage once 4 successful trials were completed. Time to cross beam was analyzed. The *Cdx2*^{Cre}; *Piezo2*$^{fl/fl\ or\ fl/-}$ animals were not run on the balance beam because of their poor motor coordination.

QUANTIFICATION AND STATISTICAL ANALYSIS

Statistical analysis was performed using Prism. All statistically tests performed are indicated in the figure legends. $p < 0.05$ was considered significant. Both non-parametric tests and parametric tests were used, depending on data normality. Additional details on sample sizes and statistical tests for each experiment can be found in the figure legends and main text.

Author Manuscript Author Manuscript Author Manuscript Author Manuscript

ADDITIONAL RESOURCES

Illustrations were designed in Adobe Illustrator and Biorender (Biorender.com).

Supplementary Material

Refer to Web version on PubMed Central for supplementary material.

ACKNOWLEDGEMENTS

We thank Maria Ericsson, Giovanni De Nola, and Shachar Dagan for advice and help with EM preparations. We thank Caiying Guo from the Janelia Research Campus for generating the *Piezo2*$^{smFP\text{-}FLAG}$ mouse. We thank Harald F. Hess and Adam Hantman for early input on this project. We thank Soha Ashrafi, Alan Emanuel, Vanessa Ruta and members of the Ginty Lab for comments on the manuscript. This work was supported by NIH grants NS097344 (DDG), MH117808 (WCAL), the Edward R. and Anne G. Lefler Center for Neurodegenerative Disorders (DDG), a Howard Hughes Medical Institute–Jane Coffin Childs Fellowship (AH), the Howard Hughes Medical Institute (SP and CSX), and a Stuart H.Q. & Victoria Quan Fellowship (QZ). Portions of the work were supported by a Foundry Award for the HMS Connectomics Core. DDG is an investigator of the Howard Hughes Medical Institute. This article is subject to HHMI's Open Access to Publications policy. HHMI lab heads have previously granted a nonexclusive CC BY 4.0 license to the public and a sublicensable license to HHMI in their research articles. Pursuant to those licenses, the author-accepted manuscript of this article can be made freely available under a CC BY 4.0 license immediately upon publication.

INCLUSION AND DIVERSITY

We support inclusive, diverse, and equitable conduct of research.

REFERENCES

1. Handler A, and Ginty DD (2021). The mechanosensory neurons of touch and their mechanisms of activation. Nat. Rev. Neurosci. 22, 521–537. 10.1038/s41583-021-00489-x. [PubMed: 34312536]
2. Bai L, Lehnert BP, Liu J, Neubarth NL, Dickendesher TL, Nwe PH, Cassidy C, Woodbury CJ, and Ginty DD (2015). Genetic Identification of an Expansive Mechanoreceptor Sensitive to Skin Stroking. Cell 163, 1783–1795. 10.1016/j.cell.2015.11.060. [PubMed: 26687362]
3. Neubarth NL, Emanuel AJ, Liu Y, Springel MW, Handler A, Zhang Q, Lehnert BP, Guo C, Orefice LL, Abdelaziz A, et al. (2020). Meissner corpuscles and their spatially intermingled afferents underlie gentle touch perception. Science (80-.). 368, 1–12. 10.1126/science.abb2751.
4. Lewin GR, and McMahon SB (1991). Physiological properties of primary sensory neurons appropriately and inappropriately innervating skin in the adult rat. J. Neurophysiol. 66, 1205–1217. 10.1152/jn.1991.66.4.1205. [PubMed: 1761980]
5. Koltzenburg M, Stucky CL, and Lewin GR (1997). Receptive properties of mouse sensory neurons innervating hairy skin. J. Neurophysiol. 78, 1841–1850. 10.1152/jn.1997.78.4.1841. [PubMed: 9325353]
6. Johansson RS, Vallbo ÅB, and Westling G (1980). Thresholds of mechanosensitive afferents in the human hand as measured with von Frey hairs. Brain Res. 184, 343–351. 10.1016/0006-8993(80)90803-3. [PubMed: 7353160]
7. Cain DM, Khasabov SG, and Simone DA (2001). Response properties of mechanoreceptors and nociceptors in mouse glabrous skin: An in vivo study. J. Neurophysiol. 85, 1561–1574. 10.1152/jn.2001.85.4.1561. [PubMed: 11287480]
8. Li L, Rutlin M, Abraira VE, Cassidy C, Kus L, Gong S, Jankowski MP, Luo W, Heintz N, Koerber HR, et al. (2011). The Functional Organization of Cutaneous Low-Threshold Mechanosensory Neurons. Cell 147, 1615–1627. 10.1016/j.cell.2011.11.027. [PubMed: 22196735]
9. Werner G, and Mountcastle VB (1965). Neural activity in mechanoreceptive cutaneous afferents: Stimulus-response relations, Weber functions, and information transmission. J. Neurophysiol. 28, 359–397. 10.1152/jn.1965.28.2.359. [PubMed: 14283062]

Author Manuscript Author Manuscript Author Manuscript Author Manuscript

10. Knibestöl M, and Vallbo B (1980). Intensity of sensation related to activity of slowly adapting mechanoreceptive units in the human hand. J. Physiol. 300, 251–267. 10.1113/jphysiol.1980.sp013160. [PubMed: 7381785]
11. Coleman GT, Bahramali H, Zhang HQ, and Rowe MJ (2001). Characterization of tactile afferent fibers in the hand of the marmoset monkey. J. Neurophysiol. 85, 1793–1804. 10.1152/jn.2001.85.5.1793. [PubMed: 11352997]
12. Harrington T, and Merzenich MM (1970). Neural coding in the sense of touch: Human sensations of skin indentation compared with the responses of slowly adapting mechanoreceptive afferents innervating the hairy skin of monkeys. Exp. Brain Res. 10, 251–264. 10.1007/BF00235049. [PubMed: 4985999]
13. Brown AG, and Iggo A (1967). A quantitative study of cutaneous receptors and afferent fibres in the cat and rabbit. J. Physiol. 193, 707–733. 10.1113/jphysiol.1967.sp008390. [PubMed: 16992307]
14. Iggo BA, and Ogawa H (1977). Correlative physiological and morphological studies of rapidly adapting mechanoreceptors in cat's glabrous skin. 266, 275–296.
15. Talbot WH, Darian-Smith I, Kornhuber HH, and Mountcastle VB (1968). The sense of flutter-vibration: comparison of the human capacity with response patterns of mechanoreceptive afferents from the monkey hand. J. Neurophysiol. 31, 301–334. 10.1152/jn.1968.31.2.301. [PubMed: 4972033]
16. Mountcastle VB, Talbot WH, Dar-Smith I, and Kornhuber HH (1967). Neural basis of the sense of flutter-vibration. Science (80-.). 155, 597–600. 10.1126/science.155.3762.597.
17. Vallbo AB, and Johansson RS (1984). Properties of cutaneous mechanoreceptors in the human hand related to touch sensation. Hum. Neurobiol. 3, 3–14. [PubMed: 6330008]
18. Roe A, Friedman R, and Chen L (2007). Multiple Representation in Primate SI: A View from a Window on the Brain. In Handbook of Neurochemistry and Molecular Neurobiology: Sensory Neurochemistry, Johnson DA and LLajtha A, eds. (Springer Science+Business Media, LLC.), pp. 1–16. 10.1007/978-0-387-30374-1.
19. Knibestöl M, and Vallbo B (1970). Single Unit Analysis of Mechanoreceptor Activity from the Human Glabrous Skin. Acta Physiol. Scand. 80, 178–195. 10.1111/j.1748-1716.1970.tb04783.x. [PubMed: 5475340]
20. Iggo A, and Muir A (1969). The structure and function of a slowly adapting touch corpuscle in hairy skin. 1882, 763–796.
21. Li L, and Ginty DD (2014). The structure and organization of lanceolate mechanosensory complexes at mouse hair follicles. Elife 3, 1–24. 10.7554/elife.01901.
22. Yamamoto T (1966). The fine structure of the palisade-type sensory endings in relation to hair follicles. J. Electron Microsc. (Tokyo). 15, 158–166. 10.1093/oxfordjournals.jmicro.a049523. [PubMed: 5965885]
23. Halata Z (1993). Sensory innervation of the hairy skin (light-and electronmicroscopic study). J. Invest. Dermatol. 101, 75S–81S. 10.1016/0022-202X(93)90505-C. [PubMed: 8326156]
24. Halata Z, and Munger BL (1980). Sensory nerve endings in rhesus monkey sinus hairs. J. Comp. Neurol. 192, 645–663. 10.1002/cne.901920403. [PubMed: 7419748]
25. Johansson RS, and Vallbo AB (1979). Tactile sensibility in the human hand: relative and absolute densities of four types of mechanoreceptive units in glabrous skin. J. Physiol. 286, 283–300. 10.1113/jphysiol.1979.sp012619. [PubMed: 439026]
26. Ranade SS, Woo SH, Dubin AE, Moshourab RA, Wetzel C, Petrus M, Mathur J, Bégay V, Coste B, Mainquist J, et al. (2014). Piezo2 is the major transducer of mechanical forces for touch sensation in mice. Nature 516, 121–125. 10.1038/nature13980. [PubMed: 25471886]
27. von Buchholtz LJ, Ghitani N, Lam RM, Licholai JA, Chesler AT, and Ryba NJP (2021). Decoding Cellular Mechanisms for Mechanosensory Discrimination. Neuron 109, 285–298.e5. 10.1016/j.neuron.2020.10.028. [PubMed: 33186546]
28. Chesler A., Szczot M., Bharucha-Goebel D., Ceko M., Donkervoort S., Laubacher C., Hayes L.., Alter K., Zampieri C., Stanley C., et al. (2016). The role of PIEZO2 in human mechanosensation. N. Engl. J. Med. 375, 1355–1364. 10.1056/NEJMoa1602812. [PubMed: 27653382]

Author Manuscript Author Manuscript Author Manuscript Author Manuscript

29. Lehnert BP, Santiago C, Huey EL, Emanuel AJ, Renauld S, Africawala N, Alkislar I, Zheng Y, Bai L, Koutsioumpa C, et al. (2021). Mechanoreceptor synapses in the brainstem shape the central representation of touch. Cell 184, 5608–5621.e18. 10.1016/j.cell.2021.09.023. [PubMed: 34637701]
30. Chirila AM, Rankin G, Tseng SY, Emanuel AJ, Chavez-Martinez CL, Zhang D, Harvey CD, and Ginty DD (2022). Mechanoreceptor signal convergence and transformation in the dorsal horn flexibly shape a diversity of outputs to the brain. Cell 185, 4541–4559.e23. 10.1016/j.cell.2022.10.012. [PubMed: 36334588]
31. Coste B, Mathur J, Schmidt M, Earley TJ, Ranade S, Petrus MJ, Dubin AE, and Patapoutian A (2010). Piezo1 and Piezo2 are essential components of distinct mechanically activated cation channels. Science (80-.). 330, 55–60. 10.1126/science.1193270.
32. Jin P, Jan LY, and Jan YN (2020). Mechanosensitive Ion Channels: Structural Features Relevant to Mechanotransduction Mechanisms. Annu. Rev. Neurosci. 43, 207–229. 10.1146/annurev-neuro-070918-050509. [PubMed: 32084327]
33. Coste B, Xiao B, Santos JS, Syeda R, Grandl J, Spencer KS, Kim SE, Schmidt M, Mathur J, Dubin AE, et al. (2012). Piezo proteins are pore-forming subunits of mechanically activated channels. Nature 483, 176–181. 10.1038/nature10812. [PubMed: 22343900]
34. Kefauver JM, Ward AB, and Patapoutian A (2020). Discoveries in structure and physiology of mechanically activated ion channels. Nature 587, 567–576. 10.1038/s41586-020-2933-1. [PubMed: 33239794]
35. Ikeda R, Cha M, Ling J, Jia Z, Coyle D, and Gu JG (2014). Merkel cells transduce and encode tactile stimuli to drive aβ-Afferent impulses. Cell 157, 664–675. 10.1016/j.cell.2014.02.026. [PubMed: 24746027]
36. Woo S, Ranade S, Weyer A, Dubin A, Baba Y, Qiu Z, Petrus M, Miyamoto T, Reddy K, Lumpkin E, et al. (2014). Piezo2 is required for Merkel-cell mechanotransduction. Nature 509, 622–626. 10.1038/nature13251. [PubMed: 24717433]
37. Woo S-H, Lumpkin EA, and Patapoutian A (2015). Merkel cells and neurons keep in touch. Trens Cell Biol 25, 74–81. 10.1016/j.pestbp.2011.02.012.Investigations.
38. Maksimovic S, Nakatani M, Baba Y, Nelson AM, Marshall KL, Wellnitz SA, Firozi P, Woo SH, Ranade S, Patapoutian A, et al. (2014). Epidermal Merkel cells are mechanosensory cells that tune mammalian touch receptors. Nature 509, 617–621. 10.1038/nature13250. [PubMed: 24717432]
39. Nakatani M, Maksimovic S, Baba Y, and Lumpkin EA (2015). Mechanotransduction in epidermal Merkel cells. Pflugers Arch. Eur. J. Physiol. 467, 101–108. 10.1007/s00424-014-1569-0. [PubMed: 25053537]
40. Viswanathan S, Williams ME, Bloss EB, Stasevich TJ, Speer CM, Nern A, Pfeiffer BD, Hooks BM, Li WP, English BP, et al. (2015). High-performance probes for light and electron microscopy. Nat. Methods 12, 568–576. 10.1038/nmeth.3365. [PubMed: 25915120]
41. Abdo H, Calvo-Enrique L, Lopez JM, Song J, Zhang MD, Usoskin D, Manira A. El, Adameyko I., Hjerling-Leffler J., and Ernfors P. (2019). Specialized cutaneous schwann cells initiate pain sensation. Science 365, 695–699. 10.1126/science.aax6452. [PubMed: 31416963]
42. Nikolaev YA, Feketa VV, Anderson EO, Schneider ER, Gracheva EO, and Bagriantsev SN (2020). Lamellar cells in Pacinian and Meissner corpuscles are touch sensors. Sci. Adv. 6.
43. Schwaller F, Bégay V, García-garcía G, Taberner FJ, Moshourab R, Mcdonald B, Docter T, Kühnemund J, Ojeda-alonso J, Paricio-montesinos R, et al. (2020). USH2A is a Meissner's corpuscle protein necessary for normal vibration sensing in mice and humans. Nat. Neurosci. 24, 74–78. 10.1038/s41593-020-00751-y. [PubMed: 33288907]
44. Andres KH (1966). Über die Feinstruktur der Rezeptoren an Sinushaaren. Zeitschrift für Zellforsch. und Mikroskopische Anat. 75, 339–365. 10.1007/BF00407165.
45. Takahashi-Iwanaga H (2000). Three-dimensional microanatomy of longitudinal lanceolate endings in rat vibrissae. J. Comp. Neurol. 426, 259–269. 10.1002/1096-9861(20001016)426:2<259::AID-CNE7>3.0.CO;2-N. [PubMed: 10982467]
46. Spencer PS, and Schaumburg HH (1973). An ultrastructural study of the inner core of the Pacinian corpuscle. J. Neurocytol. 2, 217–235. 10.1007/BF01474721. [PubMed: 4775768]

Author Manuscript Author Manuscript Author Manuscript Author Manuscript

47. Takahashi-Iwanaga H (2003). The three-dimensional microanatomy of Meissner corpuscles in monkey palmar skin. J. Neurocytol. 32, 363–371. [PubMed: 14724379]
48. García-Mesa Y, García-Piqueras J, García B, Feito J, Cabo R, Cobo J, Vega JA, and García-Suárez O (2017). Merkel cells and Meissner's corpuscles in human digital skin display Piezo2 immunoreactivity. J. Anat. 231, 978–989. 10.1111/joa.12688. [PubMed: 28905996]
49. Villarino NW, Hamed YMF, Ghosh B, Dubin AE, Lewis AH, Odem MA, Loud MC, Wang Y, Servin-Vences MR, Patapoutian A, et al. (2023). Labeling PIEZO2 activity in the peripheral nervous system. Neuron, 1–14. 10.1016/j.neuron.2023.05.015. [PubMed: 36603547]
50. Pickles JO, Comis SD, and Osborne MP (1984). Cross-links between stereocilia in the guinea pig organ of Corti, and their possible relation to sensory transduction. Hear. Res. 15, 103–112. 10.1016/0378-5955(84)90041-8. [PubMed: 6436216]
51. Howard J, and Hudspeth AJ (1988). Compliance of the hair bundle associated with gating of mechanoelectrical transduction channels in the Bullfrog's saccular hair cell. Neuron 1, 189–199. 10.1016/0896-6273(88)90139-0. [PubMed: 2483095]
52. Qiu X, and Müller U (2022). Sensing sound: Cellular specializations and molecular force sensors. Neuron 110, 3667–3687. 10.1016/j.neuron.2022.09.018. [PubMed: 36223766]
53. Xu CS, Hayworth KJ, Lu Z, Grob P, Hassan AM, García-Cerdán JG, Niyogi KK, Nogales E, Weinberg RJ, and Hess HF (2017). Enhanced FIB-SEM systems for large-volume 3D imaging. Elife 6. 10.7554/eLife.25916.
54. Nguyen TM, Thomas LA, Rhoades JL, Ricchi I, Yuan XC, Sheridan A, Hildebrand DGC, Funke J, Regehr WG, and Lee WCA (2023). Structured cerebellar connectivity supports resilient pattern separation. Nature 613, 543–549. 10.1038/s41586-022-05471-w. [PubMed: 36418404]
55. Kuehn ED, Meltzer S, Abraira VE, Ho CY, and Ginty DD (2019). Tiling and somatotopic alignment of mammalian low-threshold mechanoreceptors. Proc. Natl. Acad. Sci. U. S. A. 116, 9168–9177. 10.1073/pnas.1901378116. [PubMed: 30996124]
56. Parton RG, and Del Pozo MA (2013). Caveolae as plasma membrane sensors, protectors and organizers. Nat. Rev. Mol. Cell Biol. 14, 98–112. 10.1038/nrm3512. [PubMed: 23340574]
57. Ghitani N, Barik A, Szczot M, Thompson JH, Li C, Le Pichon CE, Krashes MJ, and Chesler AT (2017). Specialized Mechanosensory Nociceptors Mediating Rapid Responses to Hair Pull. Neuron 95, 944–954.e4. 10.1016/j.neuron.2017.07.024. [PubMed: 28817806]
58. Sharma N, Flaherty K, Lezgiyeva K, Wagner DE, Klein AM, and Ginty DD (2020). The emergence of transcriptional identity in somatosensory neurons. Nature 577, 392–398. [PubMed: 31915380]
59. Qi L, Iskols M, Shi D, Reddy P, Walker C, Lezgiyeva K, Voisin T, Pawlak M, Kuchroo VK, Chiu I, et al. (2023). A DRG genetic toolkit reveals molecular, morphological, and functional diversity of somatosensory neuron subtypes. bioRxiv, 2023.04.22.537932.
60. Zhang Q, Lee WCA, Paul DL, and Ginty DD (2019). Multiplexed peroxidase-based electron microscopy labeling enables simultaneous visualization of multiple cell types. Nat. Neurosci. 22, 828–839. 10.1038/s41593-019-0358-7. [PubMed: 30886406]
61. Paré M, Elde R, Mazurkiewicz JE, Smith AM, and Rice FL (2001). The Meissner corpuscle revised: A multiafferented mechanoreceptor with nociceptor immunochemical properties. J. Neurosci. 21, 7236–7246. 10.1523/jneurosci.21-18-07236.2001. [PubMed: 11549734]
62. Zelena J (1994). Nerves and Mechanoreceptors. Chapman Hall, ed. (Springer Netherlands).
63. Luo W, Enomoto H, Rice FL, Milbrandt J, and Ginty DD (2009). Molecular Identification of Rapidly Adapting Mechanoreceptors and Their Developmental Dependence on Ret Signaling. Neuron 64, 841–856. 10.1016/j.neuron.2009.11.003. [PubMed: 20064391]
64. Vega JA, Del Valle ME, Haro JJ, Naves FJ, Calzada B, and Uribellarea R (1994). The inner-core, outer-core and capsule cells of the human pacinian corpuscles: An Immunohistochemical study. Eur. J. Morphol. 32, 11–18. [PubMed: 7522027]
65. Kaidoh T, and Inoué T (2000). Intercellular junctions between palisade nerve endings and outer root sheath cells of rat vellus hairs. J. Comp. Neurol. 420, 419–427. 10.1002/(SICI)1096-9861(20000515)420:4<419::AID-CNE1>3.0.CO;2-3. [PubMed: 10805917]
66. Kaidoh T, and Inoué T (2008). N-Cadherin Expression in Palisade Nerve Endings of Rat Vellus Hairs. J. Comp. Neurol. 506, 525–534. 10.1002/cne.21550. [PubMed: 18067145]

Author Manuscript Author Manuscript Author Manuscript Author Manuscript

67. Yap AS, Duszyc K, and Viasnoff V (2018). Mechanosensing and mechanotransduction at cell –cell junctions. Cold Spring Harb. Perspect. Biol. 10, 1–16. 10.1101/cshperspect.a028761.
68. Mallon BS, Elizabeth Shick H, Kidd GJ, and Macklin WB (2002). Proteolipid promoter activity distinguishes two populations of NG2-positive cells throughout neonatal cortical development. J. Neurosci. 10.1523/jneurosci.22-03-00876.2002.
69. Doerflinger NH, Macklin WB, and Popko B (2003). Inducible site-specific recombination in myelinating cells. Genes. (United States). 10.1002/gene.10154.
70. Choi S, Hachisuka J, Brett MA, Magee AR, Omori Y, Iqbal N. ul A., Zhang D., DeLisle MM., Wolfson RL., Bai L., et al. (2020). Parallel ascending spinal pathways for affective touch and pain. Nature 587, 258–263. 10.1038/s41586-020-2860-1. [PubMed: 33116307]
71. Razani B, Engelman JA, Wang XB, Schubert W, Zhang XL, Marks CB, Macalusol F, Russell RG, Li M, Pestell RG, et al. (2001). Caveolin-1 Null Mice Are Viable but Show Evidence of Hyperproliferative and Vascular Abnormalities. J. Biol. Chem. 276, 38121–38138. 10.1074/jbc.M105408200. [PubMed: 11457855]
72. Rutlin M, Ho CY, Abraira VE, Cassidy C, Woodbury CJ, and Ginty DD (2014). The cellular and molecular basis of direction selectivity of Aδ-LTMRs. Cell 159, 1640–1651. 10.1016/j.cell.2014.11.038. [PubMed: 25525881]
73. Madisen L, Zwingman TA, Sunkin SM, Oh SW, Zariwala HA, Gu H, Ng LL, Palmiter RD, Hawrylycz MJ, Jones AR, et al. (2010). A robust and high-throughput Cre reporting and characterization system for the whole mouse brain. Nat. Neurosci. 13, 133–140. 10.1038/nn.2467. [PubMed: 20023653]
74. Livet J, Weissman TA, Kang H, Draft RW, Lu J, Bennis RA, Sanes JR, and Lichtman JW (2007). Transgenic strategies for combinatorial expression of fluorescent proteins in the nervous system. Nature 450, 56–62. 10.1038/nature06293. [PubMed: 17972876]
75. Snippert HJ, van der Flier LG, Sato T, van Es JH, van den Born M, Kroon-Veenboer C, Barker N, Klein AM, van Rheenen J, Simons BD, et al. (2010). Intestinal crypt homeostasis results from neutral competition between symmetrically dividing Lgr5 stem cells. Cell 143, 134–144. 10.1016/j.cell.2010.09.016. [PubMed: 20887898]
76. Coutaud B, and Pilon N (2013). Characterization of a novel transgenic mouse line expressing Cre recombinase under the control of the Cdx2 neural specific enhancer. Genesis. 10.1002/dvg.22421.
77. Nonomura K, Woo SH, Chang RB, Gillich A, Qiu Z, Francisco AG, Ranade SS, Liberles SD, and Patapoutian A (2017). Piezo2 senses airway stretch and mediates lung inflation-induced apnoea. Nature 541, 176–181. 10.1038/nature20793. [PubMed: 28002412]
78. Jaegle M, Ghazvini M, Mandemakers W, Piirsoo M, Driegen S, Levavasseur F, Raghoenath S, Grosveld F, and Meijer D (2003). The POU proteins Brn-2 and Oct-6 share important functions in Schwann cell development. Genes Dev. 17, 1380–1391. 10.1101/gad.258203. [PubMed: 12782656]
79. Huang S, O'Donovan KJ, Turner EE, Zhong J, and Ginty DD (2015). Extrinsic and intrinsic signals converge on the Runx1/CBFβ transcription factor for nonpeptidergic nociceptor maturation. Elife 4, 1–24. 10.7554/eLife.10874.
80. Pang S, and Xu CS (2023). Methods of enhanced FIB-SEM sample preparation and image acquisition. Methods Cell Biol. Vol. Electron Microsc. Vol. 181.
81. Xu CS, Pang S, Hayworth KJ, and Hess HF (2020). Transforming FIB-SEM Systems for Large-Volume Connectomics and Cell Biology. In Neuromethods 10.1007/978-1-0716-0691-9_12.
82. Xu CS, Pang S, Shtengel G, Müller A, Ritter AT, Hoffman HK, Takemura S. ya, Lu Z., Pasolli HA., Iyer N., et al. (2021). An open-access volume electron microscopy atlas of whole cells and tissues. Nature. 10.1038/s41586-021-03992-4.
83. Klein S, Staring M, Murphy K, Viergever MA, and Pluim JPW (2010). Elastix: A toolbox for intensity-based medical image registration. IEEE Trans. Med. Imaging. 10.1109/TMI.2009.2035616.
84. Shamonin DP, Bron EE, Lelieveldt BPF, Smits M, Klein S, and Staring M (2014). Fast parallel image registration on CPU and GPU for diagnostic classification of Alzheimer's disease. Front. Neuroinform. 10.3389/fninf.2013.00050.

Author Manuscript Author Manuscript Author Manuscript Author Manuscript

85. Phelps JS, Hildebrand DGC, Graham BJ, Kuan AT, Thomas LA, Nguyen TM, Buhmann J, Azevedo AW, Sustar A, Agrawal S, et al. (2021). Reconstruction of motor control circuits in adult Drosophila using automated transmission electron microscopy. Cell. 10.1016/j.cell.2020.12.013.

86. Kuan AT, Phelps JS, Thomas LA, Nguyen TM, Han J, Chen CL, Azevedo AW, Tuthill JC, Funke J, Cloetens P, et al. (2020). Dense neuronal reconstruction through X-ray holographic nano-tomography. Nat. Neurosci. 10.1038/s41593-020-0704-9.

87. Funke J, Tschopp F, Grisaitis W, Sheridan A, Singh C, Saalfeld S, and Turaga SC (2019). Large Scale Image Segmentation with Structured Loss Based Deep Learning for Connectome Reconstruction. IEEE Trans. Pattern Anal. Mach. Intell. 10.1109/TPAMI.2018.2835450.

88. Boergens KM, Berning M, Bocklisch T, Bräunlein D, Drawitsch F, Frohnhofen J, Herold T, Otto P, Rzepka N, Werkmeister T, et al. (2017). WebKnossos: Efficient online 3D data annotation for connectomics. Nat. Methods. 10.1038/nmeth.4331.

89. Lee Kisuk, Zung Jonathan, Li Peter, Jain Viren, H.S.S. (2017). Superhuman accuracy on the SNEMI3D connectomics challenge. arXiv Prepr. 10.48550/arXiv.1706.00120.

90. Jorstad A, Nigro B, Cali C, Wawrzyniak M, Fua P, and Knott G (2015). NeuroMorph: A Toolset for the Morphometric Analysis and Visualization of 3D Models Derived from Electron Microscopy Image Stacks. Neuroinformatics 13, 83–92. 10.1007/s12021-014-9242-5. [PubMed: 25240318]

91. Jorstad A, Blanc J, and Knott G (2018). NeuroMorph: A Software Toolset for 3D Analysis of Neurite Morphology and Connectivity. Front. Neuroanat. 12, 1–12.10.3389/fnana.2018.00059. [PubMed: 29440997]

Author Manuscript Author Manuscript Author Manuscript Author Manuscript

3–4 Highlights

- In end organs, Piezo2 is restricted in expression and function to sensory axons
- FIB-SEM reveals conserved ultrastructural features shared by distinct Aβ RA-LTMRs
- Aβ RA-LTMRs of each end organ contain a high density of axon protrusions
- Axon protrusions anchor to end organ Schwann cells through adherens junctions

Author Manuscript Author Manuscript Author Manuscript Author Manuscript

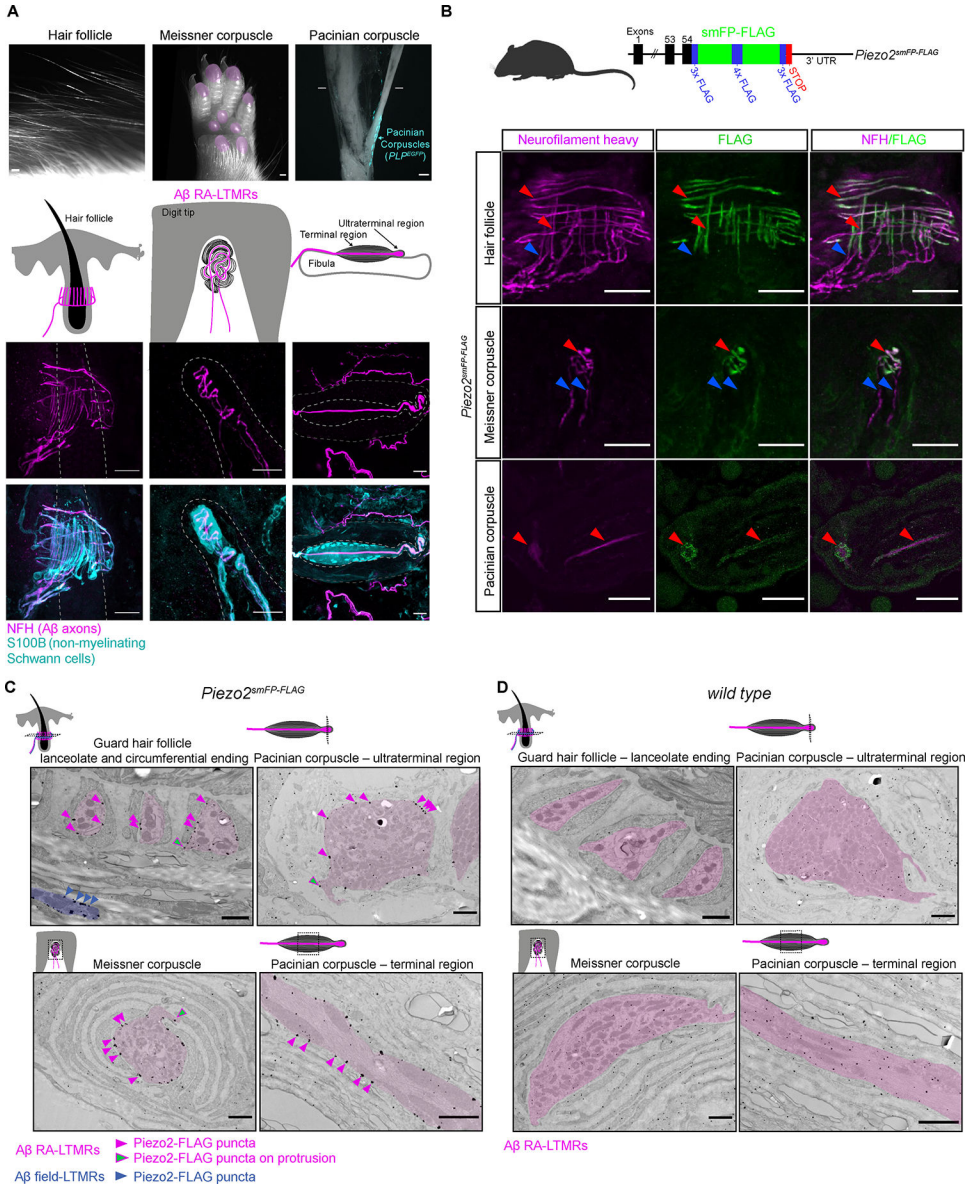

Figure 1. Piezo2 is restricted to axonal endings across morphologically dissimilar Aβ RA-LTMRs.

(**A**) Image of three main skin/tissue regions that contain end organs formed by Aβ RA-LTMRs: lanceolate endings around hair follicles, Meissner corpuscles within glabrous skin of digit tips and pedal pads (regions indicated in pink), and Pacinian corpuscles (indicated by the PLP^{EGFP} fluorescent label) around the periosteum of the fibula. Diagrams illustrate end organs with Aβ RA-LTMRs in magenta. Representative confocal images show Aβ RA-LTMRs (NFH^+) and specialized non-neuronal Schwann cells ($S100B^+$) of each end organ. Dashed lines outline the hair follicle (left), dermal papilla (middle), and boundary of outer and inner core (right). Scalebar, 20 μm.

(**B**) Top, schematic diagram of the *Piezo2*$^{smFP\text{-}FLAG}$ allele. Bottom, confocal images of Piezo2-FLAG localization to Aβ RA-LTMR axons (NFH^+) in the three end organs. Red arrowheads indicate co-localized FLAG and NFH signal. Blue arrowheads indicate axonal

Author Manuscript Author Manuscript Author Manuscript Author Manuscript

NFH signal outside the end organ that lacks FLAG signal. This experiment was repeated in two animals with littermate controls. Scalebar, 25 μm.

(**C**) Immuno-electron micrographs from a *Piezo2*$^{smFP\text{-}FLAG}$ animal stained for FLAG with silver enhancement show localization of the Piezo2-FLAG fusion protein along the membranes of Aβ RA-LTMRs (pseudo-colored pink). Pink arrowheads indicate a subset of Piezo2-FLAG puncta along sensory axon membranes; green arrowheads indicate a subset of puncta along axon protrusions. Piezo2-FLAG is also localized to the membrane of Aβ field-LTMR circumferential endings around the guard hair (blue). This experiment was repeated in two animals with littermate controls. Scalebar, 1 μm.

(**D**) Same as in (C) but for wild-type littermate of the *Piezo2*$^{smFP\text{-}FLAG}$ animal. See also Figures S1–S2.

Author Manuscript Author Manuscript Author Manuscript Author Manuscript

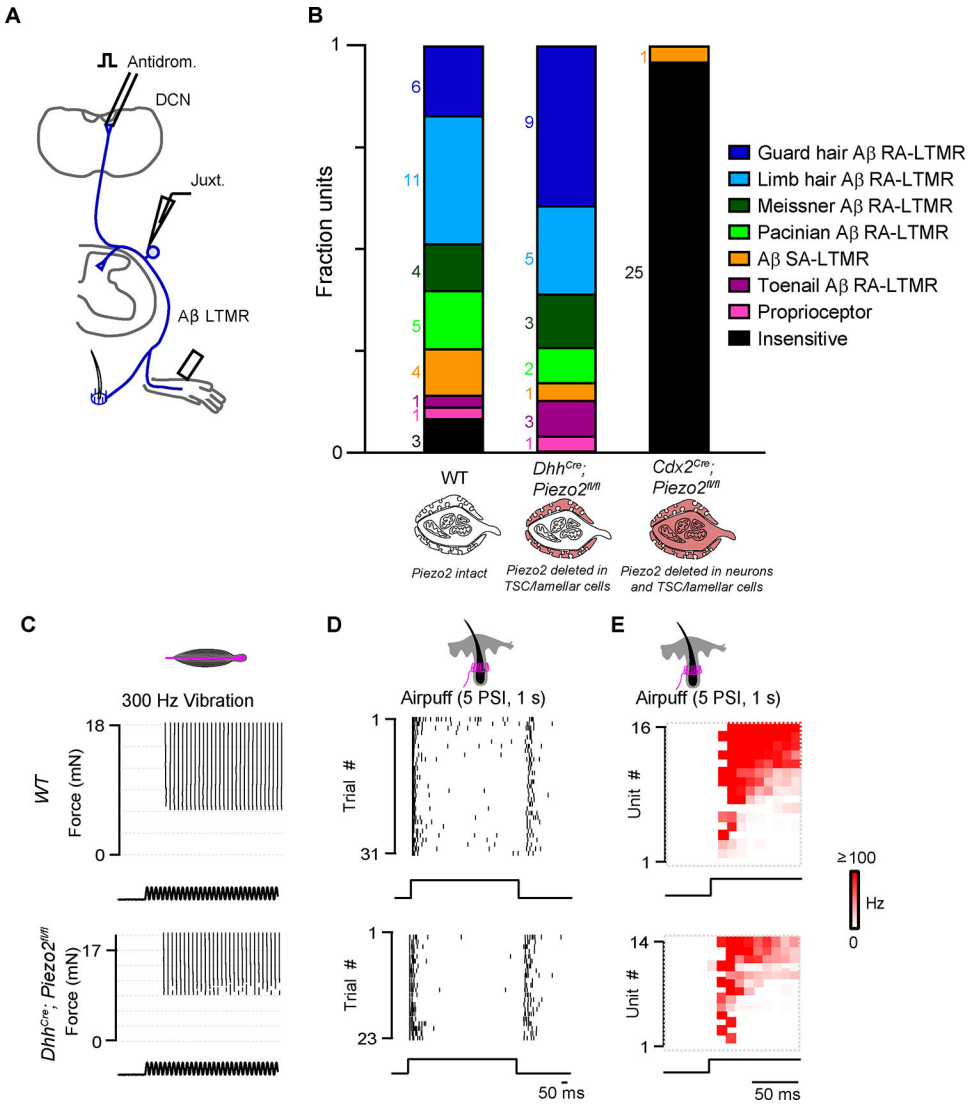

Figure 2. Deletion of Piezo2 in TSCs and lamellar cells does not affect light touch responses in Aβ sensory neurons.

(**A**) Schematic of juxtacellular recordings. Aβ sensory neurons were identified with antidromic activation of the dorsal column nucleus (DCN) or dorsal column (DC). Mechanical stimuli were applied to the hindpaw and hairy thigh.

(**B**) The fraction of DCN-projecting units identified as a specific sensory neuron class based on the location of receptive field and response to low-threshold mechanical stimuli in wild type (wt) animals (n=3), *Dhh*^{Cre};*Piezo2*$^{fl/fl}$ mice (n=3), and *Cdx2*^{Cre};*Piezo2*$^{fl/fl}$ mice (n=2).

(**C**) Raster of single Pacinian Aβ RA-LTMR responses to vibration (300 Hz) at different forces in a wt (top) and a *Dhh*^{Cre};*Piezo2*$^{fl/fl}$ animal (bottom).

(**D**) Same as in (C) but for hairy skin Aβ RA-LTMR responses to air puff.

(**E**) Histograms of air puff responses for all Aβ hairy units activated by DCN stimulation in wt (top) and *Dhh*^{Cre};*Piezo2*$^{fl/fl}$ animals (bottom). In wt animals, 15/16 hairy units were air puff-sensitive. In the *Dhh*^{Cre};*Piezo2*$^{fl/fl}$ animals, 14/15 hairy units were air puff-sensitive. See also Figure S3.

Author Manuscript Author Manuscript Author Manuscript Author Manuscript

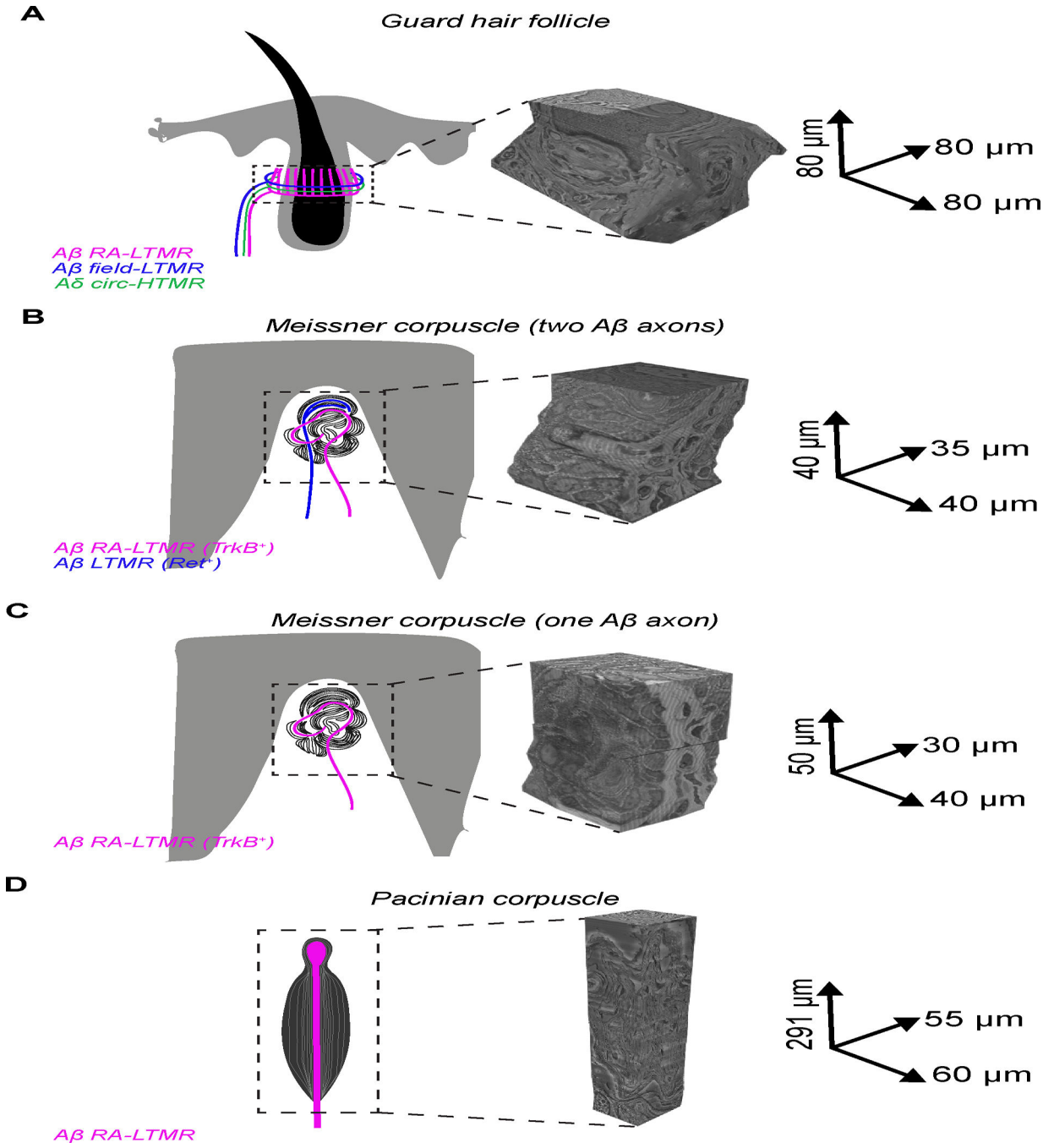

Figure 3. Aligned FIB-SEM volumes of end organs formed by Aβ RA-LTMRs.

FIB-SEM volumes with global alignment correction and dimensions for skin samples containing (**A**) a single guard hair; (**B**) a Meissner corpuscle with two myelinated afferents; (**C**) a Meissner corpuscle with a single myelinated afferent; (**D**) a Pacinian corpuscle.

Author Manuscript Author Manuscript Author Manuscript Author Manuscript

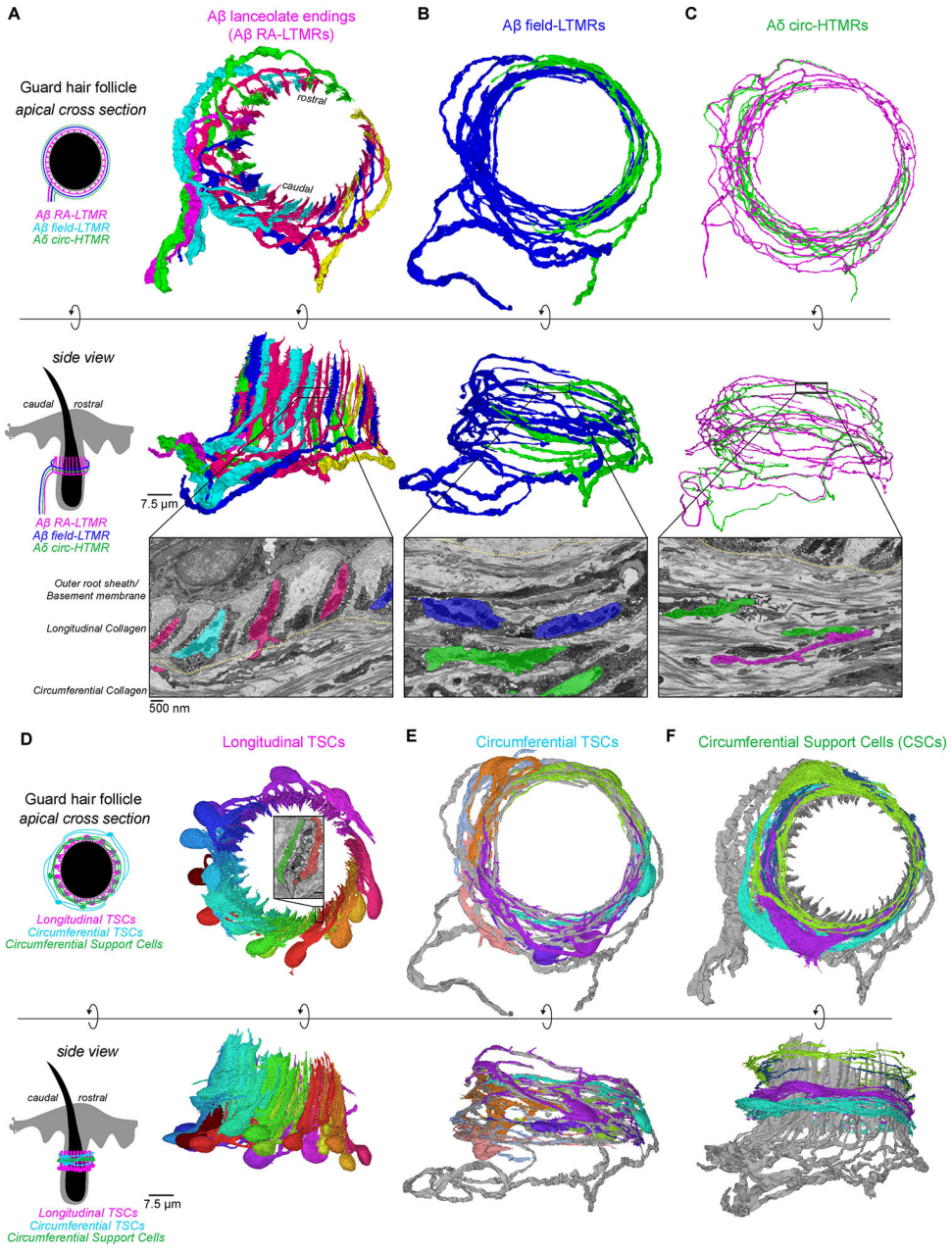

Figure 4. FIB-SEM reconstructions of Aβ and Aδ sensory neuron endings and associated non-neuronal cells of a guard hair follicle.

(**A-C**) 3D renderings of sensory neurons innervating a mouse guard hair follicle shown from an apical view (top panels) and from a side view (middle panels). Bottom panels: pseudo-colored images from FIB-SEM volume with the boundary between longitudinal and circumferential collagen matrix marked by the yellow line. (**A**) Six Aβ RA-LTMR axon segments form 47 lanceolate endings. (**B**) Two Aβ field-LTMRs and (**C**) two Aδ circ-HTMRs form circumferential endings.

(**D-F**) 3D renderings of (**D**) 17 terminal Schwann cells (TSCs) within the longitudinal collagen that form intimate associations with lanceolate endings. Inset: an example of two different TSCs associated with the same lanceolate ending; (**E**) seven circumferential TSCs

within the circumferential collagen matrix that associate with Aβ field-LTMRs (gray); (**F**) four circumferential support cells (CSCs) within the circumferential collagen matrix and frequently contact axon protrusions of Aβ RA-LTMR lanceolate endings (gray). See also Figure S4.

Author Manuscript Author Manuscript Author Manuscript Author Manuscript

Author Manuscript Author Manuscript Author Manuscript Author Manuscript

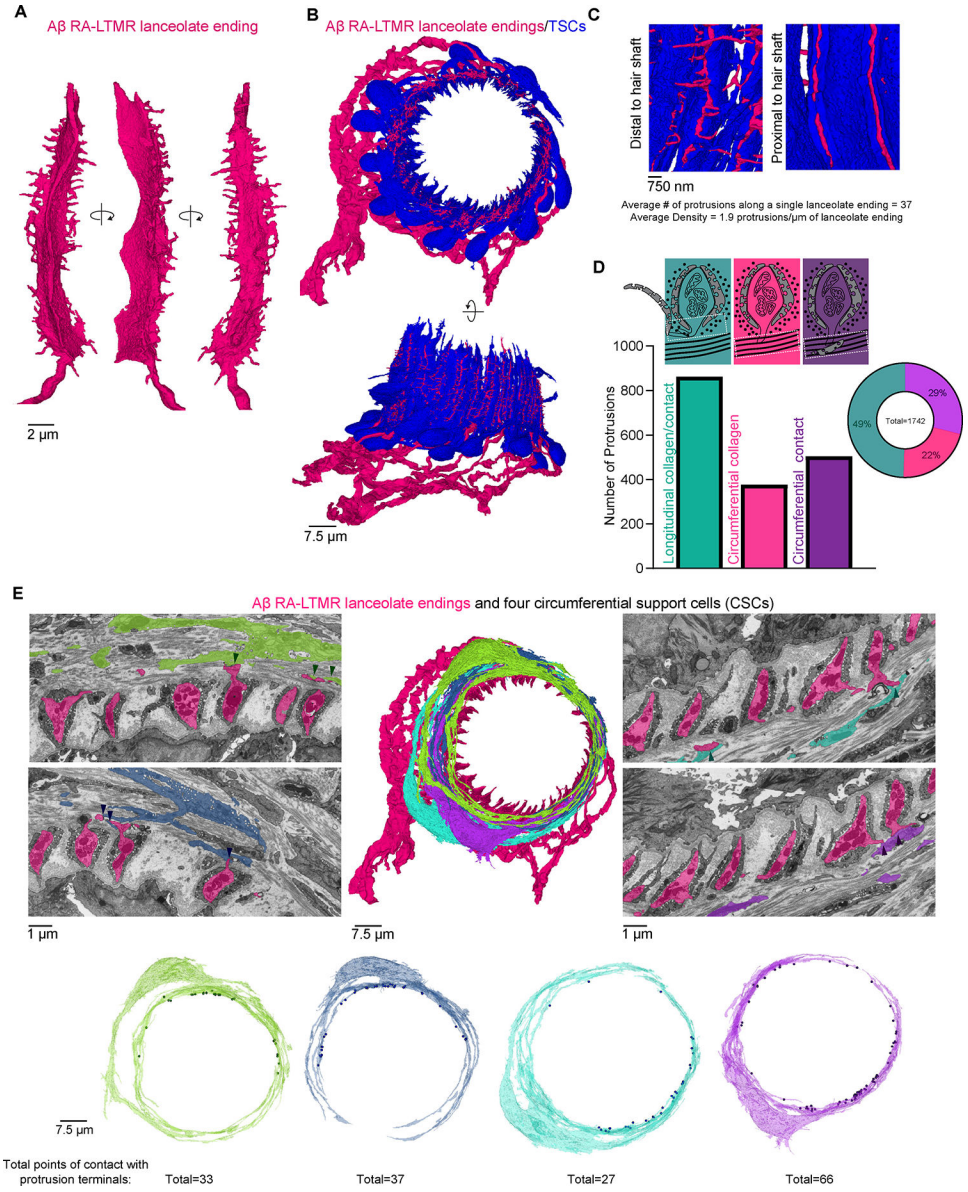

Figure 5. Axon protrusions along Aβ RA-LTMRs extend through TSC openings and contact CSCs within the guard hair's circumferential collagen network.

(**A**) A single lanceolate ending with numerous axon protrusions shown from multiple perspectives.

(**B**) Apical and side views of Aβ RA-LTMRs (magenta) and associated TSCs (blue).

(**C**) Axon protrusions emerge at TSC gaps distal to the hair shaft.

(**D**) Quantification of axon protrusion terminals. Teal: protrusions that terminate in local longitudinal collagen with or without making contact with local TSCs. Magenta: protrusions that extend into circumferential collagen but do not form cell contacts. Purple: protrusions that extend into circumferential collagen and form cell contacts.

(**E**) Axon protrusions of Aβ RA-LTMRs that extend into the circumferential collagen network frequently contact four reconstructed CSCs (arrow heads). Points where each CSC

contacts an axon protrusion are marked as dots on the 3D rendering of the cell. See also Figure S5.

Author Manuscript Author Manuscript Author Manuscript Author Manuscript

Author Manuscript Author Manuscript Author Manuscript Author Manuscript

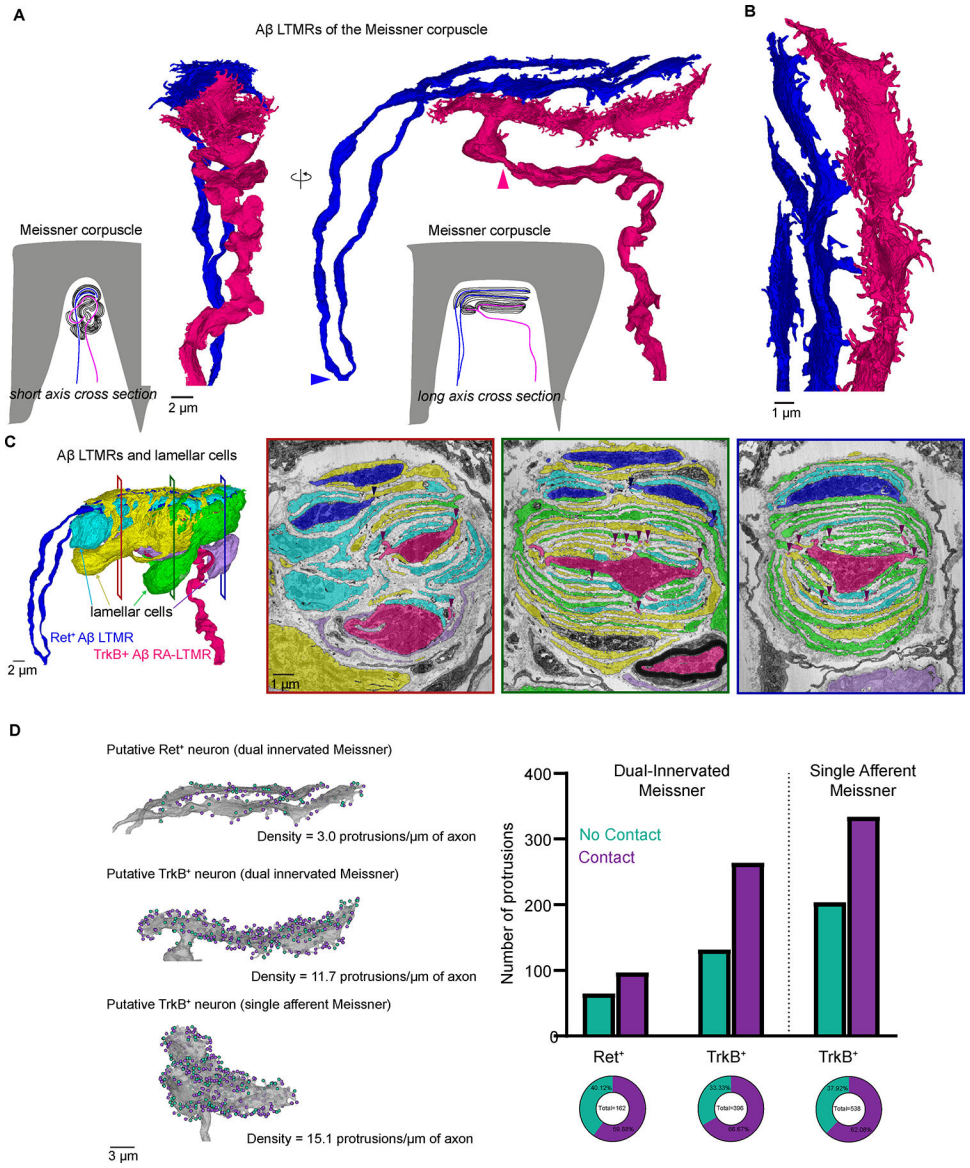

Figure 6. FIB-SEM reconstructions of two Meissner corpuscles reveal the density of axon protrusions to be a structural correlate of Aβ LTMR tactile sensitivity.

(**A**) 3D renderings of two Aβ LTMRs that innervate a Meissner corpuscle. Arrowheads indicate the termination of myelination.

(**B**) Higher magnification rendering of the terminal portion of the two Aβ LTMRs.

(**C**) Left, 3D renderings of the two Aβ LTMRs and four lamellar cells that form the Meissner corpuscle. Right, pseudo-colored images from the FIB-SEM volume at different depths across the corpuscle. Arrowheads show points where axon protrusions contact lamellar cells.

(**D**) Left, 3D renderings of the two axons from the dual-innervated corpuscle and of the axon from the single-innervated corpuscle. Teal dots indicate protrusions that terminate in the collagen (no contact). Purple dots indicate protrusions that contact lamellar cells. Right, quantification of protrusion terminals. See also Figure S6.

Author Manuscript Author Manuscript Author Manuscript Author Manuscript

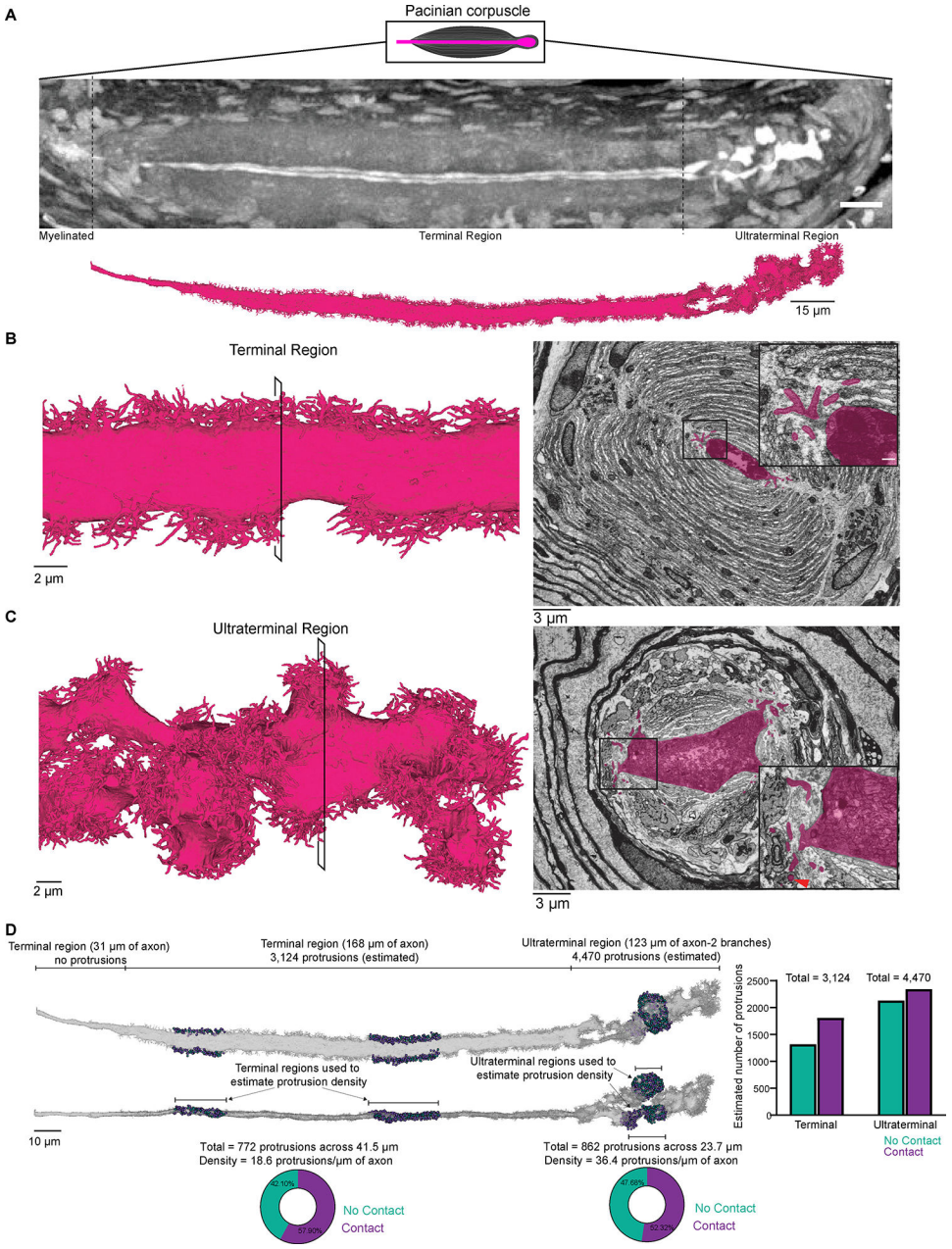

Figure 7. FIB-SEM reconstruction of a Pacinian corpuscle Aβ RA-LTMR reveals dense networks of axon protrusions that form contacts with lamellar cells.

(**A**) X-ray tomography of a Pacinian corpuscle (axon in white) prior to FIB-SEM imaging (top) and 3D rendering of the reconstructed Pacinian Aβ RA-LTMR after imaging (bottom).

(**B**) Left, 3D rendering of a section of the Aβ RA-LTMR in the terminal region. Right, pseudo-colored image from the FIB-SEM volume with inset showing protrusions and their contacts with lamellar cells.

(**C**) Same as in (B) except for the ultraterminal region. The red arrowhead indicates a protrusion encased by a lamellar cell at the inner and outer core boundary.

(**D**) Characterization of protrusion terminals in the terminal and ultraterminal region. Two representative regions in the terminal and ultraterminal region (total of 4) were selected

Author Manuscript Author Manuscript Author Manuscript Author Manuscript

to quantify and characterize protrusion terminals. The pie charts show the percentage of protrusions within these regions that contact a lamellar cell (purple) or do not form a contact (teal). The statistics of protrusion terminals in these regions were used to estimate the total number of protrusions and their termination type within both the terminal and ultraterminal region (graphed on the right). See also Figure S7.

Author Manuscript Author Manuscript Author Manuscript Author Manuscript

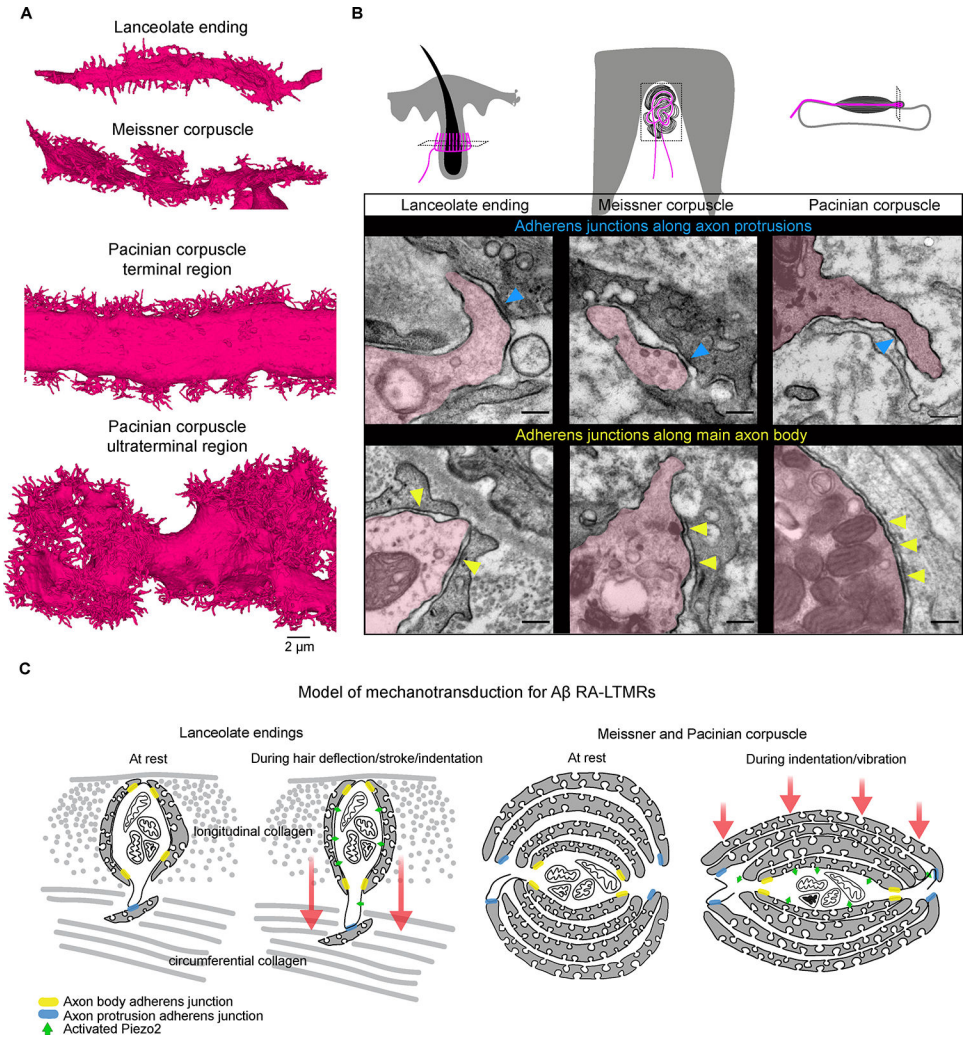

Figure 8. The conserved presence of adherens junctions along axon protrusion contacts with non-neuronal cells and a unified model of mechanotransduction.

(**A**) 3D renderings of a portion of the Aβ RA-LTMR axons from each end organ (terminal and ultraterminal region shown for the Pacinian corpuscle). Images are shown on the same scale.

(**B**) TEM micrographs processed with tannic acid and post-stain showing adherens junctions between axon protrusions of Aβ RA-LTMRs (magenta) and resident non-neuronal cells (blue arrowheads) and along the main body of the Aβ RA-LTMRs and neighboring terminal Schwann cells or lamellar cells (yellow arrowheads) in each end organ. This experiment was repeated in two animals. Scalebar, 200 nm.

(**C**) Schematic of proposed model of mechanotransduction for Aβ RA-LTMRs. Adherens junctions serve as anchor sites that render the Aβ RA-LTMR uniquely sensitive to dynamic stimuli. Hair deflection or skin indentation/vibration tugs on the hundreds to thousands of protrusions along the length of the axon within the end organ leading to stretching of the Aβ RA-LTMR membrane and activation of Piezo2. See also Figure S8.

Author Manuscript Author Manuscript Author Manuscript Author Manuscript

REAGENT or RESOURCE	SOURCE	IDENTIFIER
Antibodies		
goat anti-mCherry	Sicgen	AB0040-200
chicken anti-GFP	Aves lab	GFP-1020 RRID:AB_10000240
rabbit anti-GFP	Invitrogen	A-11122
goat anti-GFP	US Biological	G8965-01E
rabbit anti-S100 beta	ProteinTech	15146-1-AP RRID:AB_2254244
rabbit anti-TUJ1 (TUBB3)	Biolegend	802001 RRID:AB_2564645
chicken anti-neurofilament heavy chain	Aves lab	SKU: NFH RRID:AB_2313552
rabbit anti-CGRP	Immunostar	24112 RRID:AB_572217
guinea pig anti-FLAG	Huang et al., 2015	NA
Bacterial and virus strains		
Biological samples		
Chemicals, peptides, and recombinant proteins		
Tamoxifen	Sigma	T5648-1g
Sunflower seed oil	Sigma	S5007
Urethane	Sigma	U2500
Tannic acid low molecular weight	EMS	21710
Glutaraldehyde	EMS	16316
Paraformaldehyde	EMS	15712
Sodium cacodylate	EMS	12310
Calcium chloride	Sigma	793639
Magnesium chloride hexahydrate	Sigma	M9272
Glycine	Sigma	410225
3,3’-diaminobenzidine tetrahydrochloride hydrate	Sigma	D5637
Osmium tetroxide	EMS	19190
Potassium ferrocyanide	Sigma	P3289
Uranyl acetate	EMS	22400
Maleic acid	Sigma	M0375
Propylene oxide	EMS	20411
LX-112	Ladd Research	21310

Author Manuscript Author Manuscript Author Manuscript Author Manuscript

REAGENT or RESOURCE	SOURCE	IDENTIFIER
DDSA	EMS	13710
NMA	EMS	19000
DMP-30	EMS	13600
Durcupan AMC	Sigma	44610-1EA
Gelatin from cold water fish	Sigma	G7041-100G
Normal goat serum	Vector labs	S-1000
Nanogold®-Fab' Goat anti-Guinea Pig IgG (H+L)	Nanoprobes	#2055-0.5ML
HQ Silver Enhancer	Nanoprobes	#2012-45ML
Neg-50 Frozen Section Medium	VWR	21008-918
Critical commercial assays		
Deposited data		
Raw-aligned and segmented FIB-SEM volumes	This paper	Janelia's OpenOrganelle
Experimental models: Cell lines		
Experimental models: Organisms/strains		
Mouse: *Piezo2*$^{smFP\text{-}FLAG}$	This paper	By request
Mouse: *Plp1*^{EGFP}	The Jackson Laboratory	RRID:IMSR_JAX:03335
Mouse: *Plp1*^{CreER}	The Jackson Laboratory	RRID:IMSR_JAX:00597
Mouse: *ROSA26*$^{LSL\text{-}Matrix\text{-}d\ APEX2}$	The Jackson Laboratory	RRID:IMSR_JAX:03276
Mouse: *ROSA26*$^{FSF\text{-}Matrix\text{-}dAPEX2}$	The Jackson Laboratory	RRID:IMSR_JAX:03276
Mouse: *TrkC*^{CreER}	The Jackson Laboratory	RRID:IMSR_JAX:03029
Mouse: *CGRP*^{FlpE}	Choi et al., 2020	NA
Mouse: *Cav1*$^{-/-}$	The Jackson Laboratory	RRID:IMSR_JAX:00708
Mouse: *TrkB*^{CreER}	The Jackson Laboratory	RRID:IMSR_JAX:02721

Author Manuscript Author Manuscript Author Manuscript Author Manuscript

REAGENT or RESOURCE	SOURCE	IDENTIFIER
Mouse: *ROSA26*$^{FSF\text{-}LSL\text{-}tdTomato}$	The Jackson Laboratory	RRID:IMSR_JAX:02187
Mouse: *Advillin*^{FlpO}	Choi et al., 2020	NA
Mouse: *NPY2RGFP*	GENSAT	011016-UCD
Mouse: *Cdx2*^{Cre}	Coutaud et al., 2013	NA
Mouse: *Piezo2*$^{fl/fl}$	The Jackson Laboratory	RRID:IMSR_JAX:02772
Mouse: *Piezo2*^{null}	Nonomura et al., 2017	NA
Mouse: *ROSA26*$^{CAG\text{-}Brainbow2.1}$	The Jackson Laboratory	RRID:IMSR_JAX:01749
Mouse: *Dhh*^{Cre}	The Jackson Laboratory	RRID:IMSR_JAX:01292
Oligonucleotides		
gRNA: CCTTAATACGACTCACTATAGGCAAACTGATCACTTAAGACCTGGGTTTTAGAGCTAGAAATAGC	This paper	NA
gRNA: AAAAGCACCGACTCGGTGCCACTTTTTCAAGTTGATAACGGACTAGCCTTATTTTAACTTGCTATTTCTAGCTCTAAAAC	This paper	NA
Forward5' Piezo2-Exon54: TGGAACTGGAGGAAGACCTCTACG	This paper	NA
Reverse5' Piezo2-smFP-FLAG: GAACAGCTCCTCGCCTTTCG	This paper	NA
Reverse5' Piezo2-3'UTR: CCCTGATTTCAGAGACATGGGAGT	This paper	NA
Recombinant DNA		
Software and algorithms		
MATLAB	Mathworks	RRID: SCR_001622
Python	https://www.python.org/	NA
PRISM8	GraphPad	NA
Segway	Nguyen et al., 2023; Kuan et al., 2020	NA
Gunpowder	Nguyen et al., 2023	https://github.com/funkey/gunpowder/
MD-Seg	Nguyen et al., 2023	https://github.com/htem/segway.mdseg, ver. 0.1
Neuroglancer	https://github.com/htem/neuroglancer_mdsea/tree/segway_pr_v2, ver 2.17;	NA

Author Manuscript Author Manuscript Author Manuscript Author Manuscript

REAGENT or RESOURCE	SOURCE	IDENTIFIER
	forked from https://github.com/google/neuroglancer	
Elastix	https://github.com/SuperElastix/elastix; https://github.com/htem/run_elastix	NA
WebKnossos	https://github.com/scalableminds/webknossos	NA
NeuroMorph	https://neuromorph.epfl.ch/ Jorstad et al., 2015; Jorstad et al., 2018	NA
Blender	https://www.blender.org/	NA
Igneous	https://github.com/seung-lab/igneous	NA
Other		
Patch-clamp amplifier	Molecular Devices	Multiclamp 700A
Acquisition system	Molecular Devices	Digidata 1440A
TEM Microscope	JEOL	1200EX
FIB-SEM custom imaging system	Zeiss	Xu et al., 2017; Xu et al., 2020; Xu et al., 2021